nature microbiology

Article

https://doi.org/10.1038/s41564-025-01967-z

Immune targeting and host-protective effects of the latent stage of *Toxoplasma gondii*

Received: 18 August 2022

Accepted: 19 February 2025

Published online: 27 March 2025

Check for updates

Julia N. Eberhard[1,12], Lindsey A. Shallberg[1,12], Aaron Winn[2,12], Sambamurthy Chandrasekaran[3], Christopher J. Giuliano[4,5], Emily F. Merritt[6], Elinor Willis[7], Christoph Konradt[8], David A. Christian[1], Daniel L. Aldridge[1], Molly E. Bunkofske[1], Maxime Jacquet[1], Florence Dzierszinski[9], Eleni Katifori[2,10], Sebastian Lourido[4,5], Anita A. Koshy[3,6,11] & Christopher A. Hunter[1]

Latency is a microbial strategy for persistence. For *Toxoplasma gondii* the bradyzoite stage forms long-lived cysts critical for transmission, and its presence in neurons is considered important for immune evasion. However, the extent to which cyst formation escapes immune pressure and mediates persistence remained unclear. Here we developed a mathematical model highlighting that bradyzoite-directed immunity contributes to control of cyst numbers. In vivo studies demonstrated that transgenic $CD8^+$ T cells recognized a cyst-derived antigen, and neuronal STAT1 signalling promoted cyst control in mice. Modelling and experiments with parasites unable to form bradyzoites (*Δbfd1*) revealed that the absence of cyst formation in the central nervous system did not prevent long-term persistence but resulted in increased tachyzoite replication with associated tissue damage and mortality. These findings suggest the latent form of *T. gondii* is under immune pressure, mitigates infection-induced damage and promotes survival of host and parasite.

Many infections lead to an asymptomatic state with low levels of micro-organism persistence despite generation of protective immunity. For some, persistence is linked to transition from a lytic to a non-lytic quiescent state that can be difficult to treat. These latent forms are considered an evolutionarily conserved strategy for immune evasion, while reactivation can cause disease and enhanced transmission,[1–6] but a lack of models has limited the ability to test how latency impacts persistence[7,8]. For the parasite *Toxoplasma gondii*, the highly replicative tachyzoite transforms to the slow-growing bradyzoite which forms long-lived cysts predominantly in neurons[4,9–11]. This switch is mediated by the transcription factor BFD1 and the RNA binding protein BFD2[12–14]. The cyst stage facilitates oral transmission and is considered important for immune evasion: two features that contribute to the evolutionary success of *T. gondii*[15].

T. gondii provides a model of natural host–pathogen interactions in mice, and the parasite's genetic tractability allows studies to dissect immune resistance to this organism[16,17]. Acute infection is dominated by dissemination of tachyzoites which replicate in many cell types, causing extensive tissue damage. With the onset of protective immunity dominated by T-cell production of IFNγ, the chronic phase is characterized by cyst formation in the central nervous system (CNS)[10,11]. While cysts had been considered dormant and the cyst wall impermeable, their relationship with the host cell is dynamic[18–20]. Cyst burden and size change over time, and periodic reactivation which releases tachyzoites can contribute to recrudescence and cause disease in patients with immune deficiencies that affect T cells[11,21–23]. Resistance to *T. gondii* is marked by a balance between limiting tissue

A full list of affiliations appears at the end of the paper. e-mail: chunter@vet.upenn.edu

damage from tachyzoite replication and immune pathology associated with this infection[24–29].

Many features of the brain contribute to its immune-privileged status[30,31]. Neurons are major histocompatibility complex (MHC) class I^{low} and show reduced responsiveness to IFNγ, which may underlie their ability to shelter pathogens[31–34]. This perspective is challenged by reports that CD8$^+$ T cells can kill virally infected neurons and evidence of non-cytopathic IFNγ-mediated mechanisms of viral clearance[35–39]. Previous reports suggested that IFNγ did not control *T. gondii* in neurons[40], but extended incubation of neurons with IFNγ does limit tachyzoite growth[34]. While T-cell production of IFNγ mediates resistance to *T. gondii*[41], there is also evidence that CD8$^+$ T cells can recognize tachyzoite-infected neurons[42,43] and that cytotoxicity contributes to CNS parasite control[44,45]. Whether cysts are directly targeted by CD8$^+$ T cells is unknown, but microglia and CD8$^+$ T cells can interact with the cyst stage[46–50]. In mice, CNS cyst burden peaks during weeks 3–5 of infection, followed by a decline in cyst numbers[18,21,51,52]. Whether cyst reactivation allows the immune response to eliminate tachyzoites and limit formation of new cysts or there is a direct mechanism to eliminate bradyzoites is unclear.

The ability to quantify T-cell responses and changes in parasite burden during toxoplasmosis has formed the basis for mathematical models describing different facets of this infection[53–56]. No existing model accounts for the possibility of immune-mediated cyst removal. In this Article, ordinary differential equations (ODEs) were developed to understand how the immune response to different developmental stages of *T. gondii* might influence parasite burden in the CNS. This model suggested immune responses targeting tachyzoites and bradyzoites lead to cyclic parasite growth and control, and inclusion of cyst lysis and reactivation dampens these oscillations. For most realistically small values of the cyst lysis rate, cyst immune clearance is necessary to produce the experimentally observed rise and fall in cyst numbers. To test the predicted roles of cyst formation and cyst-directed immunity, transgenic parasites with stage-specific expression of the model antigen OVA, parasites unable to form cysts, and mice with blunted neuronal IFNγ signalling were used. These studies revealed a CD8$^+$ T-cell response against the latent form of *T. gondii* and that the cyst provides a replicative sink required to mitigate tissue damage, thereby promoting survival of host and parasite.

Results

Modelling stage-specific immunity to *T. gondii* in the CNS

A model was developed to investigate the relationship in the CNS between tachyzoite replication, cyst formation, reactivation and immunity. These relationships are represented with populations shown as circles and reactions as squares (Fig. 1a). The corresponding system of ODEs is given in equations (1)–(3).

$$\frac{dI_T}{dt} = \beta_T I_T + \beta_B I_B - d_T I_T - \psi_T \frac{I_T Z}{S_0} - c_{TB} I_T \quad (1)$$

$$\frac{dI_B}{dt} = -d_B I_B - \psi_B \frac{I_B Z}{S_0} + c_{TB} I_T \quad (2)$$

$$\frac{dZ}{dt} = a_T \frac{I_T Z}{S_0} + a_B \frac{I_B Z}{S_0} - \mu Z \quad (3)$$

Detailed derivation of the ODEs, explanation of rate constants and comparison to the previous model are provided (Supplementary Text Section 1). The approach is similar to that in ref. 53 but considers the possibility of immune pressure on bradyzoites. The numbers of tachyzoite-infected cells, bradyzoite-infected cells and immune cells are denoted I_T, I_B and Z, respectively. The number of infected cells remains much less than the total number of cells in the CNS, so it is assumed the uninfected cell number S_0 remains constant. I_T increases at a rate $\beta_T I_T$, while tachyzoite to bradyzoite differentiation occurs at a rate $c_{TB} I_T$. Bradyzoite to tachyzoite reactivation occurs at a rate $\beta_B I_B$. Cells infected with tachyzoites or bradyzoites may rupture (at a rate $d_T I_T$ or $d_B I_B$) or be cleared by immune cells (at a rate $\psi_T I_T Z/S_0$ or $\psi_B I_B Z/S_0$). Tachyzoite- or bradyzoite-infected cells trigger the immune response at a rate $a_T I_T Z/S_0$ or $a_B I_B Z/S_0$. Feedback between the immune response and infection mirrors a predator–prey interaction: without immune pressure, parasite growth is unrestricted, but when immune cells are present, they limit parasite replication. Immune cell death occurs at a rate μZ. In Fig. 1a, the two arrows from β_T to I_T represent a +1 increase in parasite numbers, and similarly, two arrows are used to represent the ability of infected cells (a_T/a_B) to amplify the immune response (Z).

Equations (1)–(3) were solved to demonstrate the expected infection dynamics resulting from the presence or absence of cyst lysis and cyst immune clearance. Model parameters were estimated based on the literature[18,21,57–67] and our experimental data (Supplementary Text Section 4 and Supplementary Table 1). Setting certain parameters to zero illustrates several key scenarios (Fig. 1b). When the immune response is disabled (top row), numbers of tachyzoite-infected cells grow exponentially, even if bradyzoite differentiation and reactivation are incorporated (Supplementary Text Section 2). The inclusion of only anti-tachyzoite immune responses (ψ_T; second row) results in the initial exponential growth of infected cells that triggers recruitment of immune cells, then a subsequent reduction in infected cells and contraction of the immune response. This is followed by cycles of tachyzoite recrudescence and control, apparent as oscillations in tachyzoite-infected cell number (Supplementary Text Section 3.1). Inclusion of bradyzoite differentiation without reactivation (middle panel) predicts a stepped increase in bradyzoite numbers with each reactivation event. The inclusion of bradyzoite differentiation and reactivation without anti-cyst immune responses results in monotonic growth of cysts (right-hand panel). Increasing d_B leads to a rise and fall in cyst numbers, although this is only observed for a small range of biologically relevant values (Supplementary Text Section 3.2).

In the final simulations (bottom row), tachyzoite- and bradyzoite-specific immune responses are incorporated. Inclusion of differentiation without reactivation (bottom middle panel) results in oscillations in infected cell number which increase in magnitude with time (Supplementary Text Section 3.3). When bradyzoite differentiation and reactivation are integrated, dampened oscillations in infected cell number are found (bottom right-hand panel). While rupture and immune clearance can cause a decline in cyst numbers, rupture leads to a steady value of cysts, whereas immune clearance leads to a decline in cyst numbers followed by oscillations in cyst populations.

This model implies that differentiation and reactivation are necessary to dampen oscillations in infected cell number and immune cell infiltration, and incorporation of a small bradyzoite immune response markedly reduces the number of infected cells (Supplementary Text Section 5.2). These models illustrate that to recapitulate qualitative features of this infection (a rise then fall in the number of tachyzoite- and bradyzoite-infected cells), one must understand the interaction between bradyzoites and the immune system. Below we provide evidence consistent with a_B and $\psi_B > 0$ by demonstrating that CD8$^+$ T cells and IFNγ are activated by and exert pressure on bradyzoite-infected cells.

Cyst-derived antigen induces a CD8$^+$ T-cell response

To determine whether CD8$^+$ T cells recognize cyst-derived antigens, parasites were generated expressing the model antigen OVA under a bradyzoite-specific promoter (bag1-OVA), and these were compared to parasites expressing OVA in tachyzoites and bradyzoites[68] (tub1-OVA; Fig. 2a). The transfer of OT-I T cells (transgenic CD8$^+$ T cells that recognize the SIINFEKL epitope of OVA) allowed a comparison of the ability of these strains to activate CD8$^+$ T cells. Microscopy

https://doi.org/10.1038/s41564-025-01967-z

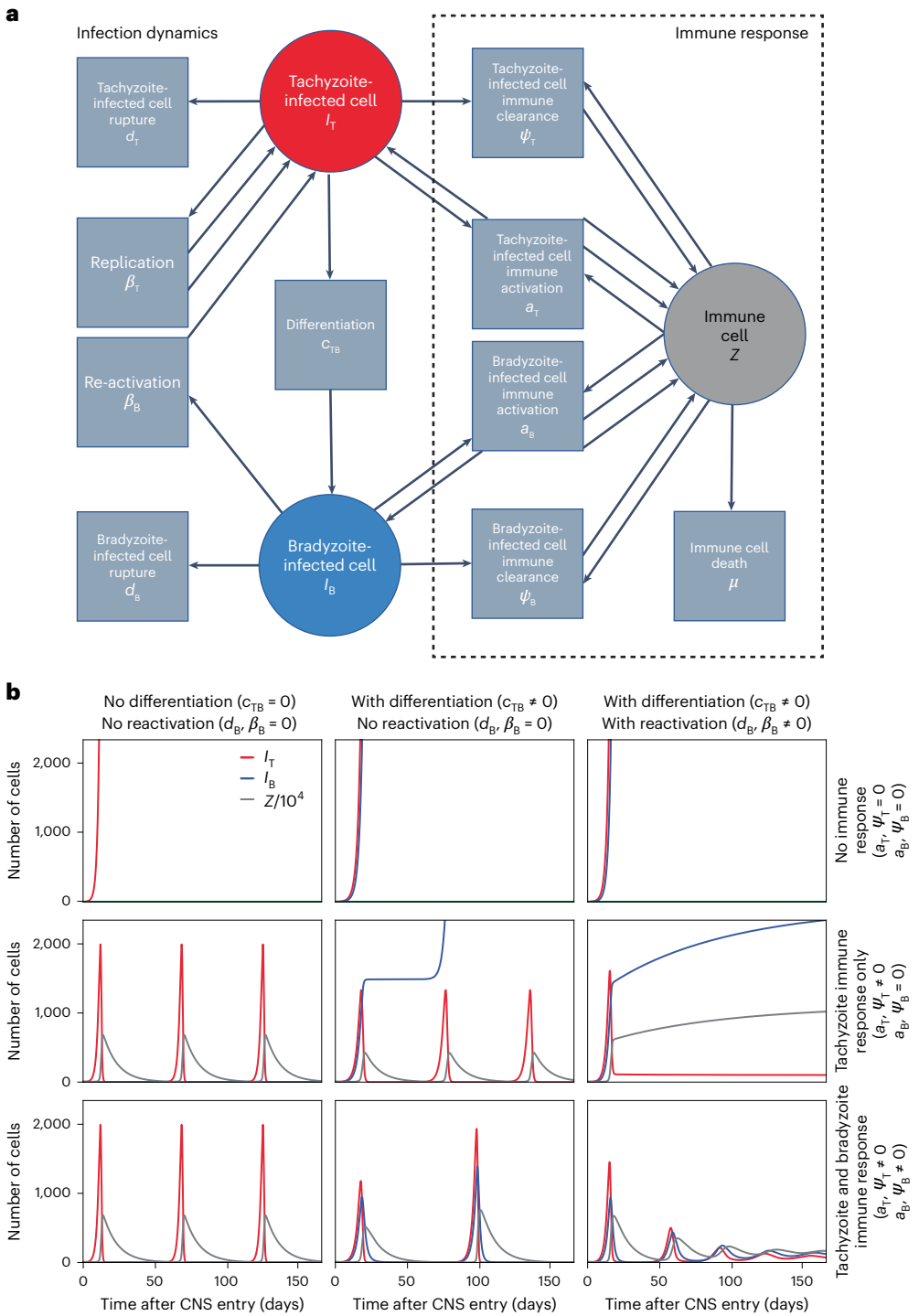

Fig. 1 | Compartmental modelling of *T. gondii* infection in the CNS predicts the presence of immune responses to tachyzoites and bradyzoites. a, Petri net representing the infection (left) and immune response (right) dynamics in equations (1)–(3). Circles represent different cell populations: tachyzoite- (I_T, red) or bradyzoite-infected (I_B, blue) cells and immune cells (Z, grey). Squares represent a particular reaction. Arrows entering a square represent reactants, and those leaving represent products. The two arrows from β_T to I_T represent a +1 increase in parasite numbers, and similarly, two arrows from α_T (α_B) to Z represent the ability of tachyzoite (bradyzoite)-infected cells to amplify the immune response. **b**, Graphical representations of potential outcomes for the numbers of tachyzoite-infected cells (I_T, red), bradyzoite-infected cells (I_B, blue) and immune cells (Z, grey) after parasite entry into the CNS, based on equations (1)–(3). Columns show different parasite dynamics: no parasite differentiation nor reactivation ($c_{TB} = 0$ and $d_B, \beta_B = 0$; left column), differentiation but no reactivation ($c_{TB} \neq 0$ and $d_B, \beta_B = 0$; middle column), or both differentiation and reactivation ($c_{TB} \neq 0$ and $d_B, \beta_B \neq 0$; right column). Rows show different immune responses: no immune response ($a_T, \psi_T = 0$ and $a_B, \psi_B = 0$; top row), immune responses against tachyzoites only ($a_T, \psi_T \neq 0$ and $a_B, \psi_B = 0$; middle row), or immune responses against tachyzoites and bradyzoites ($a_T, \psi_T \neq 0$ and $a_B, \psi_B \neq 0$; bottom row). When nonzero, the parameters used were $S_0 = 10^8$, $I_T(0) = 1$, $I_B(0) = 0$, $Z(0) = 10^5$, $d_T = 0.2$, $d_B = 0.01$, $\beta_T = 1.7$, $\beta_B = 0.2$, $c_{TB} = 0.25$, $a_T = 10^5$, $a_B = 0.2 \times 10^5$, $\mu = 0.1$, $\psi_T = 50$, $\psi_B = 10$.

https://doi.org/10.1038/s41564-025-01967-z

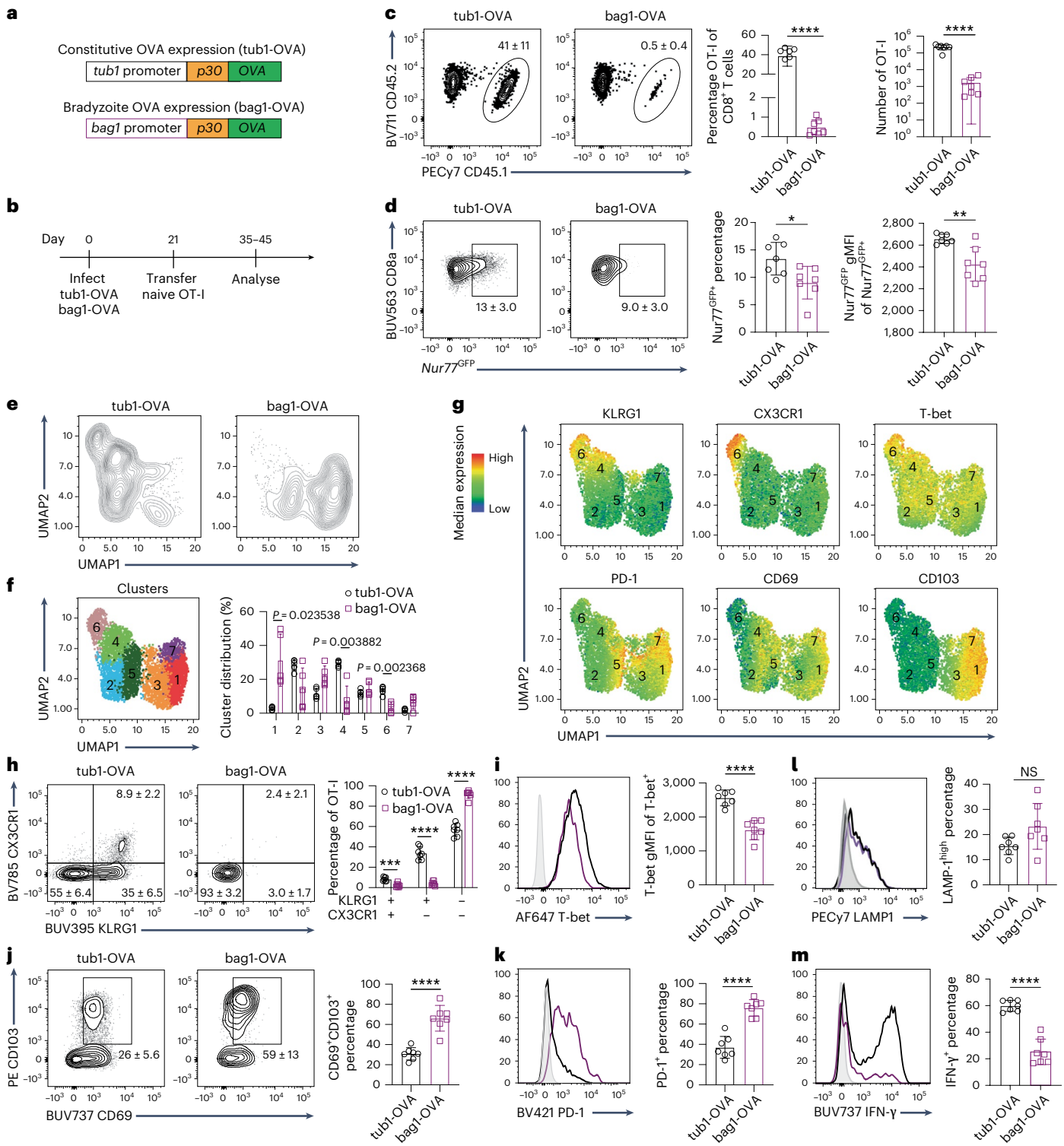

Fig. 2 | Cyst-derived antigen induces a CD8$^+$ T-cell response in the CNS. **a**, Transgenic parasite constructs for constitutive (tub1-OVA) and bradyzoite (bag1-OVA) restricted OVA expression. Expression of truncated OVA was linked to the secretion signal p30 and driven by either the *TUB1* or *BAG1* promoter. **b**, Experimental design for **c**–**m**. C57BL/6J mice were infected with tub1-OVA or bag1-OVA parasites ($n = 7$ mice per group). At 21 d.p.i., naive congenically distinct (CD45.1$^+$CD45.2$^+$) Nur77^{GFP} OT-I T cells were transferred intravenously. Brains were collected at 35–45 d.p.i., and OT-I T cells were analysed by flow cytometry. **c**, Frequency and number of OT-I T cells (****$P < 0.0001$). **d**, Frequency and geometric mean fluorescence intensity (gMFI) of Nur77^{GFP} expression in OT-I T cells shown in **c** (*$P = 0.0176$, **$P = 0.0024$). **e**,**f**, UMAP analysis (**e**) and unsupervised clustering (**f**) of OT-I T cells pooled from tub1-OVA and bag1-OVA infected brains. Colours represent 7 individual clusters identified through X-shift clustering analysis. **g**, Heat maps showing MFI of individual phenotypic markers across the 7 clusters identified in **f**. **h**–**k**, Flow cytometric profiling of OT-I T cells based on expression of KLRG1 and CX3CR1 (**h**), T-bet (**i**), CD69 and CD103 (**j**) and PD-1 (**k**). Grey histogram sample indicates expression by naive CD8$^+$ T cells (in **h**, ***$P = 0.000311$, ****$P < 0.00001$; in **i**, ****$P < 0.0001$; in **j**, ****$P < 0.0001$; in **k**, ****$P < 0.0001$). **l**,**m**, OT-I degranulation (**l**) and intracellular IFN-γ staining (**m**) after 4 h restimulation with SIINFEKL peptide. Grey indicates unstimulated OT-I T-cell controls (in **m**, ****$P < 0.0001$). Data are representative plots from three independent experiments. Data analysed by two-sided unpaired Student's *t*-test. Bonferroni–Dunn correction for multiple comparisons included in statistical analyses performed in **f** and **h**. NS, $P > 0.05$. Bar graphs depict the mean ± s.d.

https://doi.org/10.1038/s41564-025-01967-z

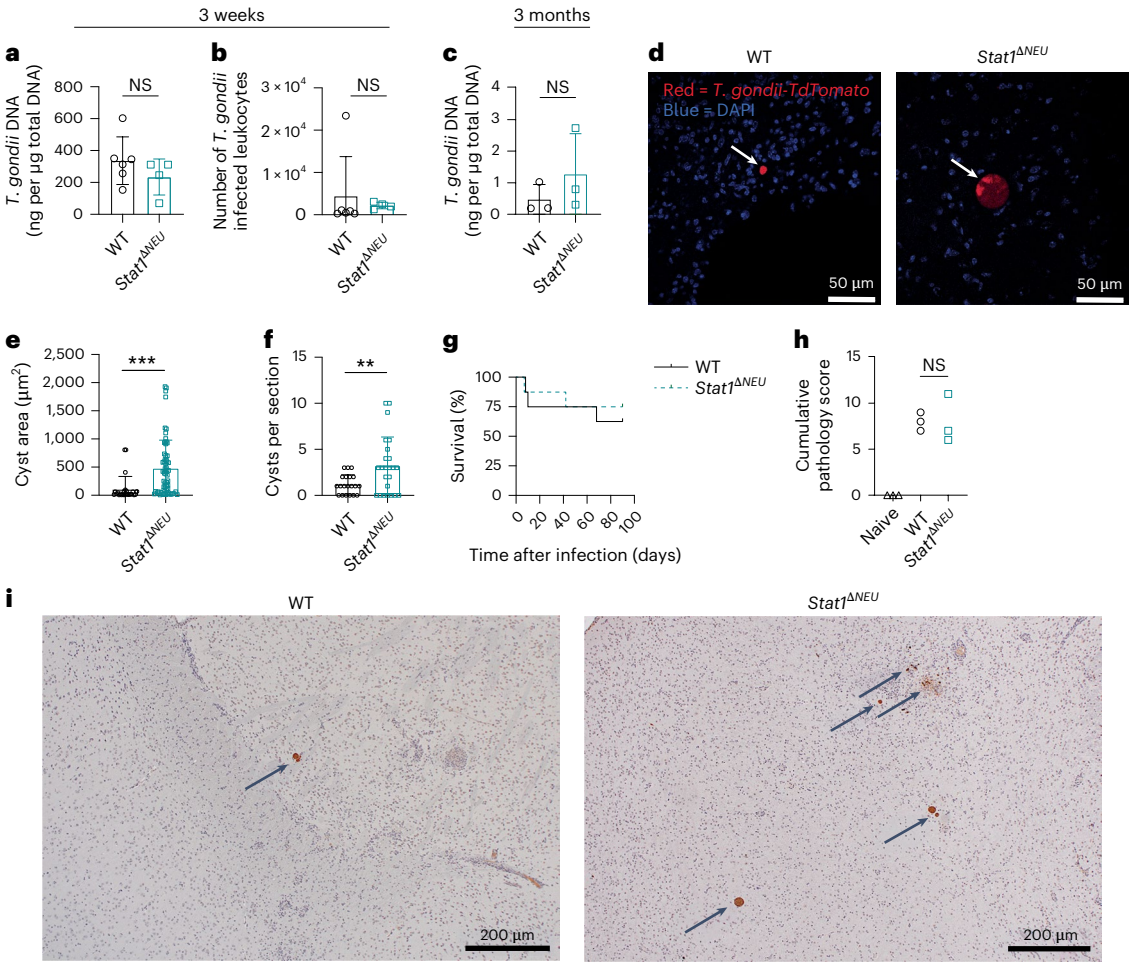

Fig. 3 | Neuronal STAT1 mediates cyst control during chronic *T. gondii* infection. C57BL/6J (WT) and *Stat1*$^{\Delta NEU}$ mice were infected with tdTomato$^+$ *T. gondii* parasites, and brains were analysed at 3 weeks post-infection (w.p.i.; in **a** and **b**) or 3 m.p.i. (in **c**–**f**, **h** and **i**). **a**,**b**, Quantification of CNS parasite burden at 3 w.p.i. by qPCR (**a**) and flow cytometry for tdTomato$^+$ tachyzoite-infected CD45$^+$ leukocytes (**b**; WT, $n = 6$ mice; *Stat1*$^{\Delta NEU}$, $n = 4$ mice). **c**, Quantification of CNS parasite burden at 3 m.p.i. by qPCR ($n = 3$ mice per group). **d**, Fluorescent imaging of brains at 3 m.p.i. (tdTomato$^+$ parasites (red), DAPI (blue) and white arrows indicate *T. gondii* cysts; scale bars, 50 µm). **e**,**f**, Brain cyst area (**e**; ***$P = 0.0006$) and number (**f**; **$P = 0.0091$) at 3 m.p.i. (WT, $n = 5$ mice; *Stat1*$^{\Delta NEU}$, $n = 6$ mice). Cysts were identified as vacuoles with >32 parasites. **g**, Survival of infected WT and *Stat1*$^{\Delta NEU}$ mice ($n = 8$ mice per group). **h**, Cumulative semiquantitative pathological scores of brain sections at 3 m.p.i. ($n = 3$ mice per group). **i**, IHC for *T. gondii* on sections from the brains scored in **h**. Images depict the cerebrum and midbrain (WT) or cerebrum (*Stat1*$^{\Delta NEU}$). Arrows indicate *T. gondii* cysts (scale bars, 200 µm). Data are representative plots from two independent experiments. Data analysed by two-sided unpaired Student's *t*-test in **a**–**c**,**e** and **f** or two-sided Mann–Whitney test in **h**; NS, $P > 0.05$. Bar graphs depict the mean ± s.d.

with bag1-OVA parasites confirmed cyst-specific expression of OVA (Extended Data Fig. 1a). During acute infection, these strains established comparable parasite burdens and endogenous parasite-specific CD4$^+$ and CD8$^+$ T-cell responses (Extended Data Fig. 1b,c), but only tub1-OVA induced endogenous SIINFEKL-specific T cells (Extended Data Fig. 1b). Infection was also induced 1 day after transfer of congenically distinct CD45.1$^+$CD45.2$^+$ OT-I T cells that express Nur77^{GFP} upon T-cell receptor (TCR) engagement (Extended Data Fig. 1d,e)[48]. OT-I T cells expanded and were present in the brain and spleen at 14 days post-infection (d.p.i.) with tub1-OVA, but not bag1-OVA. At 28 d.p.i., when cyst formation occurs in the CNS, both infections resulted in OT-I T cells in the brain (Extended Data Fig. 1f). A subset of these cells were Nur77^{GFP+} (Extended Data Fig. 1g). The OT-I T-cell response in the CNS was approximately 50-fold greater during tub1-OVA infection than bag1-OVA infection (Extended Data Fig. 1f). This difference could reflect altered priming due to delayed OVA expression in bag1-OVA parasites. To normalize for time of priming, OT-I T cells were transferred into mice at 21 d.p.i. (when both parasite strains are expected to express OVA) and analysed 2–3 weeks later (Fig. 2b). The OT-I T-cell response induced by bag1-OVA remained lower in magnitude and showed a lower frequency of Nur77^{GFP+} cells (Fig. 2c,d). These data suggest that priming kinetics do not account for differences in magnitude of the OT-I T-cell response or levels of TCR engagement between tub1-OVA and bag1-OVA parasites.

We next compared OT-I T cells in the CNS responding to tub1-OVA or bag1-OVA parasites using Uniform Manifold Approximation and Projection (UMAP) analysis. This approach revealed seven clusters with varied expression of effector T-cell markers (KLRG1, CX3CR1, T-bet), inhibitory receptors (PD-1) and tissue residency markers (CD69, CD103) (Fig. 2e–g). OT-I T cells responding to tub1-OVA showed heterogenous effector phenotypes with KLRG1$^+$CX3CR1$^+$, KLRG1$^+$CX3CR1$^-$ and KLRG1$^-$CX3CR1$^-$ populations that were T-bet^{hi} (Fig. 2h,i). A small subset were CD69$^+$CD103$^+$ or PD-1^{hi} (Fig. 2j,k). By contrast, OT-I T cells responding to bag1-OVA were dominated by a KLRG1$^-$CX3CR1$^-$ population with decreased T-bet expression. These cells also co-expressed tissue resident memory markers (CD69$^+$CD103$^+$) and high levels of PD-1 (Fig. 2h–k). When OT-I T cells from infected brains were stimulated with the SIINFEKL peptide, there were similar levels of degranulation (a measure of cytotoxic potential), but those responding to bag1-OVA had reduced IFNγ production (Fig. 2l,m). These results reveal a sub-population of

https://doi.org/10.1038/s41564-025-01967-z

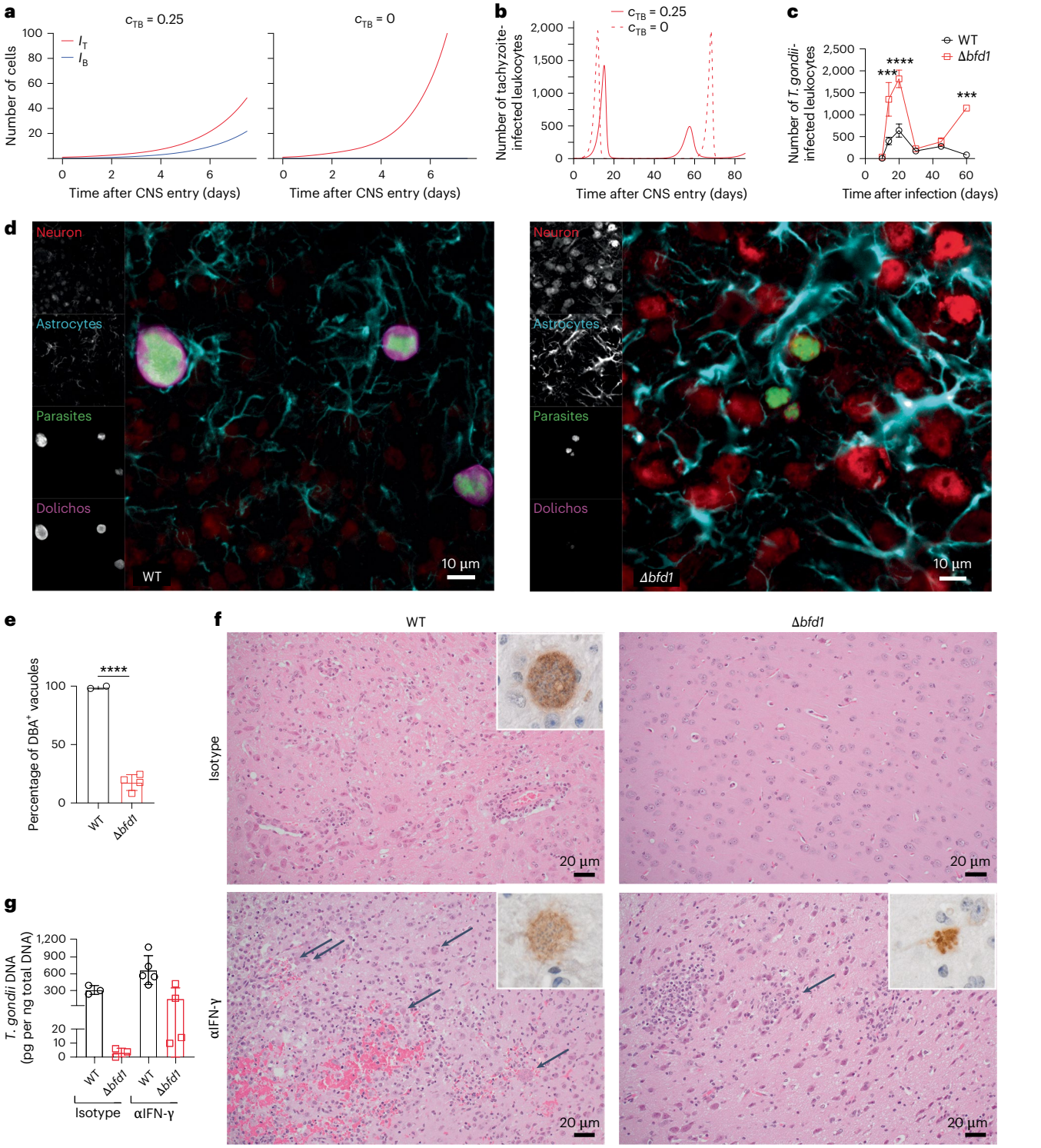

Fig. 4 | Latent stage conversion is not necessary for chronic infection. **a**,**b**, Model predictions of CNS infection dynamics with or without parasite conversion from tachyzoites to bradyzoites (c_{TB}). **a**, Early dynamics of CNS tachyzoite (I_T, red) and bradyzoite (I_B, blue) infected cells with cyst conversion (c_{TB} = 0.25; left) or without (c_{TB} = 0; right). **b**, Long-term dynamics of CNS tachyzoite infected populations with c_{TB} = 0.25 or c_{TB} = 0. **c**–**g**, C57BL/6J mice were infected with WT or Δ*bfd1* parasites. Brains were collected and analysed as described. **c**, Quantification of tdTomato$^+$ tachyzoite-infected CD45$^+$ leukocytes in the brain, analysed by flow cytometry (WT-infected, n = 3 or 4 mice per time point; Δ*bfd1*-infected, n = 3 or 5 mice per time point; ***P = 0.0017, ****P = 0.0004; data representative of 2 independent experiments). **d**, Fluorescent imaging of neurons, astrocytes, *T. gondii* parasites and cysts in the brain at 25 d.p.i. (NeuN, MAP2 and neurofilament (red); GFAP (cyan); tdTomato$^+$ *T. gondii* (green); DBA (magenta). Scale bars, 10 µm). **e**, Percentage normalization of DBA-stained vacuoles at 25 d.p.i. (WT, n = 2 vacuoles; bfd1KO, n = 4 vacuoles; ****P = <0.0001). **f**,**g**, WT- and Δ*bfd1*-infected mice were treated with 200 µg per dose of isotype (WT-infected, Δ*bfd1*-infected, n = 3 mice) or α-IFNγ antibody (WT-infected, n = 5 mice; Δ*bfd1*-infected, n = 4 mice) twice per week for 4 weeks before collection at 6 m.p.i. (data representative of 1 experiment). **f**, Representative H&E photomicrographs of brains from infected mice at 6 m.p.i. (brainstem, upper left; cerebrum, all other panels). Arrows indicate areas of *T. gondii* tachyzoite burden. Insets show cysts (upper left) or tachyzoites (lower left and right); IHC for *T. gondii*. Scale bars, 20 µm. **g**, Quantification of CNS parasite burden at 6 m.p.i. by qPCR. Data analysed by two-way ANOVA in **c** or two-sided unpaired Student's *t*-test in **e**. Line graph depicts the mean ± s.e.m. Bar graphs depict the mean ± s.d.

CD8$^+$ T cells induced and maintained by cyst-derived antigen with a distinct phenotype and reduced effector capacity.

Neuronal STAT1 mediates cyst control

The cytokine IFNγ signals through STAT1 to mediate resistance to *T. gondii*[41,69], and deletion of *Stat1* in microglia or astrocytes results in increased parasite replication and immune infiltration in the CNS[70,71]. To test the role of IFNγ in controlling *T. gondii* in neurons, *Snap25*^{Cre}-*Stat-1*$^{flox/flox}$ mice (*Stat1*$^{\Delta NEU}$) with blunted neuronal IFNγ signalling were infected. At 20 d.p.i., before extensive cyst formation, wild-type (WT) and *Stat1*$^{\Delta NEU}$ mice showed no difference in total parasite burden or numbers of infected leukocytes in the CNS (Fig. 3a,b). At 3 months post-infection (m.p.i.), parasite burden remained comparable between WT and *Stat1*$^{\Delta NEU}$ mice (Fig. 3c), but cysts in *Stat1*$^{\Delta NEU}$ brains were larger (indicative of longevity) and more numerous (Fig. 3d–f). This elevated cyst burden was not associated with increased mortality (Fig. 3g), and there were no signs of increased tachyzoite replication or associated tissue pathology (Fig. 3h,i). There were also no alterations in the numbers or phenotype of parasite-specific CD8$^+$ T cells in the CNS (Extended Data Fig. 2a–f). These results indicate that neuronal STAT1 underlies a mechanism of cyst control in vivo, consistent with $\psi_B > 0$ in our model.

Cyst formation is not required for parasite persistence

While inclusion of tachyzoite-to-bradyzoite conversion in the model produced infection dynamics that mirrored natural infection (Fig. 1), the inability to form bradyzoites ($c_{TB} = 0$) produced increased numbers of tachyzoite-infected cells early after parasite invasion of the CNS (Fig. 4a). In this scenario, parasite numbers were controlled as infection progressed; however, even in the absence of cyst formation, tachyzoites persisted and underwent periodic recrudescence as immunity waned (Fig. 4b). To test this experimentally, tub1-OVA parasites lacking BFD1 (Δ*bfd1*), a master regulator of tachyzoite to bradyzoite transition[12], were generated. At 14 d.p.i., mice infected with WT or Δ*bfd1* parasites had comparable parasite burden, splenic T-cell responses and serum IFNγ levels (Extended Data Fig. 3a–c). However, higher levels of tachyzoite-infected cells were present in the brains of Δ*bfd1*-infected mice at 14 and 21 d.p.i., followed by a contraction from 30 to 45 d.p.i. and in this experiment a recrudescence at 60 d.p.i. (Fig. 4c). The cyst wall binding reagent dolichos biflorus agglutinin (DBA$^+$) was readily detected on parasitophorous vacuoles in WT-infected mice, whereas most parasitophorous vacuoles in Δ*bfd1*-infected mice were DBA$^-$ (Fig. 4d,e). The fraction of DBA$^+$ Δ*bfd1* parasitophorous vacuoles showed weaker DBA staining than WT parasitophorous vacuoles, and Δ*bfd1* parasites within these DBA^{low} vacuoles were Sag1$^+$ (a tachyzoite surface antigen) and SRS9$^-$ (a bradyzoite surface antigen). Conversely, WT parasites within DBA$^+$ vacuoles were Sag1$^-$SRS9$^+$ (Extended Data Fig. 3d). Thus, Δ*bfd1* parasites do not form cysts in the brain.

To determine whether cyst formation is required for parasite persistence, the brains of surviving WT- and Δ*bfd1*-infected mice were examined at 6 m.p.i. WT-infected mice exhibited encephalitis, obvious cysts and quantifiable parasite burden (Fig. 4f,g). By contrast, Δ*bfd1*-infected mice lacked overt signs of inflammation or parasite replication, although low parasite burden was detectable (Fig. 4f,g). Treatment of survivors with anti-IFNγ resulted in increased parasite burden in the brains of WT- and Δ*bfd1*-infected mice at 6 m.p.i., associated with enhanced parasite replication. (Fig. 4f,g). Thus, cyst formation maintains a higher parasite burden in the CNS, but it is not essential for long-term persistence of *T. gondii*.

Cyst formation is host protective

While WT- and Δ*bfd1*-infected mice had similar initial rates of survival, Δ*bfd1*-infected mice showed increased mortality at 20–40 d.p.i. (Fig. 5a). Treatment of these mice with sulfadiazine (which inhibits tachyzoite replication) starting at 21 d.p.i. enhanced survival (Fig. 5a). Histopathological assessment of Δ*bfd1*-infected brains at 30 d.p.i. showed areas of severe tissue necrosis surrounding foci of tachyzoite replication (Fig. 5b,c). By contrast, WT-infected brains, despite the presence of inflammation and gliosis, did not show necrosis or remarkable tissue damage (Fig. 5b,c). Differences in additional indicators of CNS pathology were also apparent in WT- and Δ*bfd1*-infected brains (Extended Data Fig. 4a,b). These data indicate that higher mortality during Δ*bfd1* infection is associated with enhanced levels of tachyzoite replication.

One explanation for increased CNS tachyzoite replication during Δ*bfd1* infection could be a reduced local immune response. However, Δ*bfd1*-infected mice had increased CNS immune infiltration at 20–45 d.p.i. compared to WT-infected mice (Fig. 5d and Extended Data Fig. 4c). By 60 d.p.i., immune infiltration was similar between groups (Fig. 5d). Comparison of immune infiltrates at 30 d.p.i. revealed a similar composition between WT and Δ*bfd1* infection (Fig. 5e,f and Extended Data Fig. 4d). The only difference was an increase in the population of inflammatory monocytes during Δ*bfd1* infection (Fig. 5f–h). Phenotypic analysis was also performed after transfer of OT-I T cells 1 day before infection with WT or Δ*bfd1* parasites constitutively expressing OVA. At 14 and 30 d.p.i. OT-I T cells in the brain were phenotypically similar between infections (Extended Data Fig. 4e), although at 30 d.p.i. with Δ*bfd1* parasites there were reductions in CD69$^+$CD103$^+$ and KLRG1$^-$CX3CR1$^-$ memory-like populations (Extended Data Fig. 4f,g). These results suggest that despite a competent immune response in the CNS, increased tachyzoite replication in the brain during Δ*bfd1* infection leads to host mortality. In additional studies with BALB/c mice, which are resistant to toxoplasmic encephalitis[72,73], Δ*bfd1*-infected mice showed increased CNS immune infiltration, neuropathology and necrosis but not increased mortality or total parasite burden (Extended Data Fig. 5a–f). A recent study also showed that CBA mice infected with a cyst-defective type III strain of *T. gondii* had higher tachyzoite burdens that were capable of reactivation at 5 m.p.i. (ref. 14). These studies highlight that across toxoplasmic encephalitis models, abrogation of cyst formation is associated with increased tachyzoite replication and CNS pathology.

Discussion

While neurons represent a refuge from the immune response for many pathogens, neurons infected with viruses or *T. gondii* tachyzoites can be recognized by CD8$^+$ T cells[35,42,74]. However, the role of CD8$^+$ T cells in controlling the latent stage of *T. gondii* is less understood. There are reports that depletion of CD8$^+$ T cells in chronically infected mice does not impact cyst numbers[75], whereas others have shown that perforin-deficient mice have increased cyst numbers[44]. In addition, in severe combined immunodeficiency (SCID) mice the transfer of CD8$^+$ T cells from infected mice led to a perforin-dependent reduction in cyst numbers[45,50]. Nevertheless, it is unclear whether CD8$^+$ T-cell-mediated reduction of cysts is due to tachyzoite control or lysis of cyst-infected neurons. Intravital imaging has revealed CD8$^+$ T cells arrested near cysts, but direct interactions with and lysis of bradyzoite-infected neurons have not been observed[46–48,55]. Here, we demonstrate through (1) generation of CD8$^+$ T-cell responses against cyst-derived antigen and (2) increased cyst burden with ablation of neuronal STAT1 that there is immune-mediated recognition and control of *T. gondii* cysts. These findings, combined with modelling of host–parasite dynamics, suggest that tachyzoite clearance and bradyzoite-directed immune pressure are required to produce the progressive reduction in cyst numbers typical for this infection[21,51].

These studies are currently unable to distinguish whether there are T-cell responses primed against tachyzoites that can respond to antigens also expressed by bradyzoites[76], but nevertheless our findings raise questions about the mechanisms underlying CD8$^+$ T-cell recognition of cyst antigens. The ability of neurons to upregulate MHC class I might allow infected neurons to present cyst-derived antigen to CD8$^+$ T cells. Alternatively, reactivation could release cyst-derived

https://doi.org/10.1038/s41564-025-01967-z

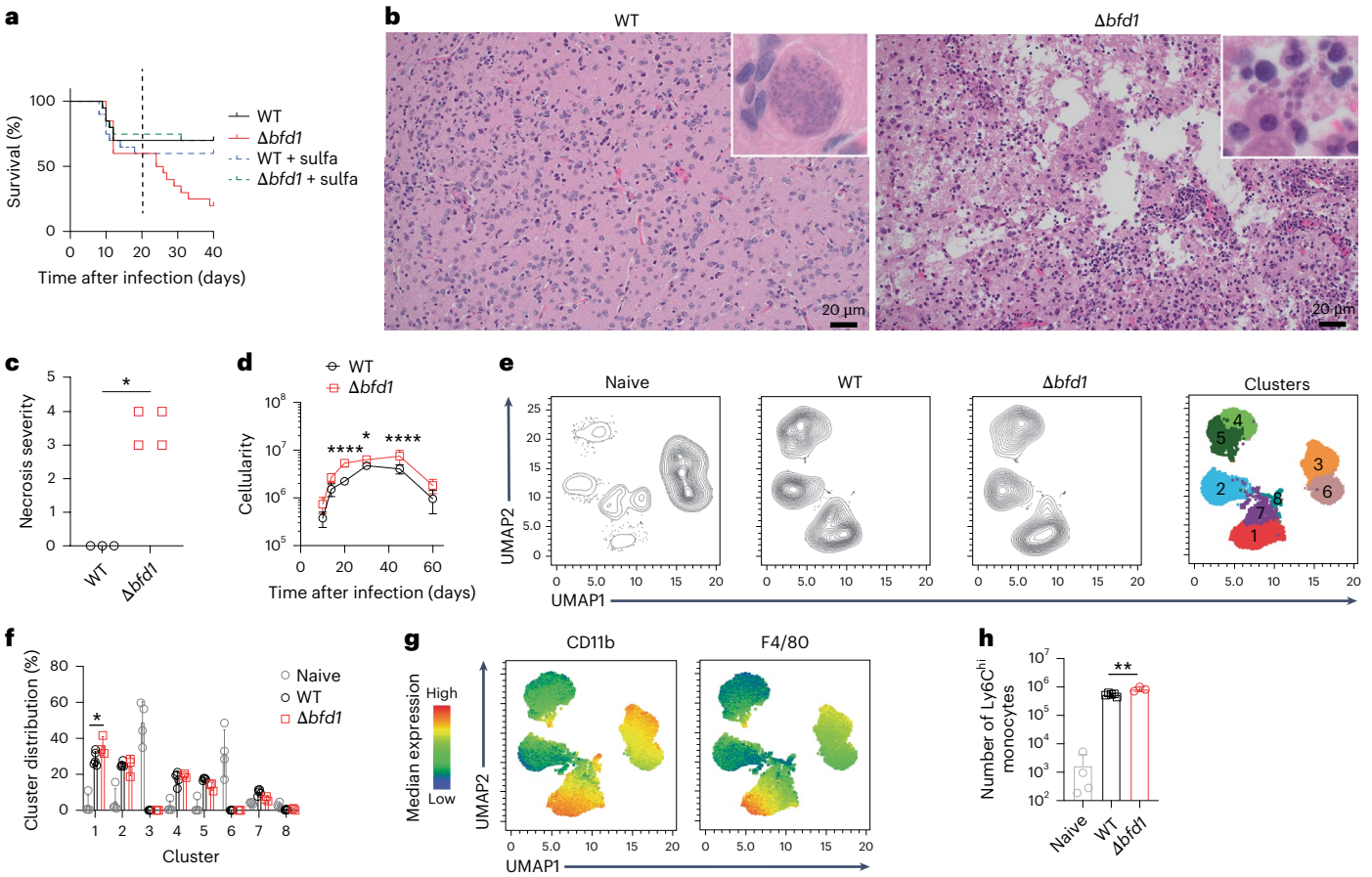

Fig. 5 | *Δbfd1* infected mice die of tachyzoite replication despite a competent immune response. a, Survival of C57BL/6J mice infected with WT ($n = 40$ mice) or *Δbfd1* ($n = 40$ mice) parasites. A subset of surviving mice received sulfadiazine treatment beginning at 21 d.p.i. (WT, $n = 12$ mice; *Δbfd1*, $n = 15$ mice; treatment start indicated by vertical dashed line; data representative of 3 independent experiments). **b**, Representative photomicrographs of WT-infected or *Δbfd1*-infected cerebra at 30 d.p.i. Insets show *T. gondii* cysts in WT-infected brains and tachyzoites in *Δbfd1*-infected brains (H&E; scale bars, 20 µm). **c**, Semiquantitative scoring of necrosis severity in brain sections at 30 d.p.i. (WT, $n = 3$ mice; *Δbfd1*, $n = 4$ mice; $^*P = 0.0286$). **d**, Brain leukocyte cellularity during chronic infection with WT ($n = 3$ or 4 mice per time point) or Δ*bfd1* ($n = 3$ or 5 mice per time point) parasites, quantified by Guava ViaCount assay ($^*P = 0.0142$, $^{****}P = <0.0001$; data representative of 2 independent experiments). **e**–**h**, Flow cytometry analysis of the brains of naive mice ($n = 4$ mice) and mice at 30 d.p.i. with WT ($n = 5$ mice) or *Δbfd1* ($n = 3$ mice) parasites (data representative of 3 independent experiments). **e**, UMAP and unsupervised x-shift clustering analysis of CNS CD45$^+$ leukocytes at 30 d.p.i. **f**, Distribution of leukocytes among the 8 clusters shown in **e** ($^*P = 0.0001$). **g**, Heat maps showing MFI of phenotypic markers with the highest expression in cluster 1. **h**, Quantification of inflammatory monocytes in the brain (CD45^{high}CD11b$^+$F4/80$^+$Ly6C^{hi}, cluster 1 shown in **e**; $^{**}P = 0.0085$). Data analysed by two-sided Mann–Whitney test in **c**, two-way ANOVA in **d**, two-sided unpaired Student's *t*-test with Bonferroni–Dunn correction for multiple comparisons in **f** and two-sided unpaired Student's *t*-test in **h**. Bar graphs depict the mean ± s.d. Line graph depicts the mean ± s.e.m.

antigens for cross-presentation by local microglia or dendritic cells. We favour a model analogous to some viral systems where local T-cell activation and production of IFNγ provides sustained signals to help neurons control infection[36,38,39,77]. Non-cytopathic IFNγ-mediated control may explain the presence of neurons that had previously been infected with *T. gondii* but cleared the parasite[78]. Many IFNγ-mediated anti-microbial mechanisms contribute to the control of tachyzoites[79], and the immunity-related GTPases have been implicated in the ability of a subset of neurons to clear *T.* gondii[34], but the relevance of these mechanisms to bradyzoite control is uncertain.

This study focused on the mechanisms involved in cyst control, but the persistence of cysts despite immune pressure suggests that this stage can mitigate immune effector responses. Consistent with this idea is bradyzoite production of the STAT1 antagonist TgIST[80–82], which suggests this stage is under selective pressure from IFNγ. In addition, the CD8$^+$ T-cell responses to cyst-derived antigen from bag1-OVA parasites comprised an unanticipated, phenotypically distinct sub-population of CD69$^+$CD103$^+$PD1^{hi} cells with a reduced ability to produce IFNγ. Other studies on CD8$^+$ T cells during toxoplasmic encephalitis have identified a T_{rm}-like (CD69$^+$CD103$^+$) subset and shown expression of PD-1 (refs. 43,46,71,83), which limits T-cell activation and production of IFNγ[84]. Because neurons express low levels of MHC class I, lack costimulatory molecules and express PD-L1 (refs. 85,86), it is possible that CD8$^+$ T-cell interactions with infected neurons lead to sub-optimal T-cell responses which could underlie the attrition, but incomplete elimination, of cysts.

The use of ODE models to understand host–pathogen dynamics provides an opportunity to manipulate aspects of host–parasite interactions in ways that are not always accessible through experimentation[87,88]. The lack of tractable models has made it hard to test how latency impacts other pathogens[7], but the computational approaches described here can be adapted to incorporate strain or pathogen-specific features associated with *T. gondii* or other infections. For example, differences in the rate of cyst formation or ability of different stages to evade the immune response can be accounted for by adjusting model parameters (c_{TB}) or (ψ_T or ψ_B). ODE models have limitations (Supplementary Text Section 6), and neglecting stochastic effects fails to predict the variety of possibilities with small infected cell

numbers. Likewise, cyst reactivation is asynchronous in vivo, and these models do not reflect differences in spatially distinct regions when recrudescence occurs. Implementation of agent-based computational models[56] could address these issues and provide more granular insights into the contributions of different immune cell populations to CNS infection dynamics. Nevertheless, the combination of modelling and in vivo experiments in this study provides insight into the interplay between the latent stage of *T. gondii* and host immune responses. Cyst development provides a replicative sink that tempers tachyzoite expansion in the CNS and prevents damage to the host, illustrating the concept that avirulence is a key feature of the parasitic lifestyle[89–91]. Thus, *T. gondii* cyst formation represents a trade-off between quiescence, which limits parasite replication, and delayed differentiation, which risks damage to the host.

Methods

Mice

Mice were housed in the University of Pennsylvania Department of Pathobiology vivarium according to institutional guidelines with 12 h light/dark cycles, ambient temperature ranging from 20 °C to 25 °C and ambient humidity ranging from 35% to 55%. C57BL/6J (stock number 000664, RRID:IMSR_JAX:000664), CD45.1 (B6.SJL-*Ptprc*^{a} *Pepc*^{b}/BoyJ, stock number 002014, RRID:IMSR_JAX:000664), *Nur77*^{GFP} (stock number 016617, RRID:IMSR_JAX:016617), OT-I (stock number 003831, RRID:IMSR_JAX:003831) and BALB/c (stock number 000651, RRID:IMSR_JAX:000651) mice were purchased from Jackson Laboratories and bred at the University of Pennsylvania. *Snap25*^{Cre} mice were generously provided by H. Zeng at the Allen Institute for Brain Science, and *Stat1*$^{flox/flox}$ mice were generously provided by L. Hennighausen at the National Institutes of Health[92]. *Snap25*^{Cre} mice were bred with *Stat1*$^{flox/flox}$ mice at the University of Pennsylvania to generate *Snap25*^{Cre}-*Stat1*$^{flox/flox}$ (*Stat1*$^{\Delta NEU}$) progeny. Cohorts of male mice were used for all studies, and all mice are on a C57BL/6 background unless otherwise noted. Ethical oversight of all animal studies was approved by the University of Pennsylvania Institutional Care and Use Committee (protocol 805045.)

Infections and T-cell transfers

T. gondii parasites were maintained in culture in human foreskin fibroblasts (HFFs). HFFs were purchased from American Type Culture Collection and were periodically tested for mycoplasma contamination using the MycoScope PCR Mycoplasma Detection Kit (Genlantis, catalogue number MY01050.) To isolate tachyzoites for infection, *T. gondii*-infected HFFs were gently scraped from flasks, passed 5 times through a 26G syringe and washed with PBS. Mice were infected at 8 weeks of age by intraperitoneal injection with 5,000 tachyzoite parasites grown in vitro.

For OT-I T-cell transfers, whole splenocytes from Naive Nur77^{GFP} CD45.1^{+}CD45.2^{+} OT-I mice were processed as described below. The fraction of OT-I cells in the splenocytes was determined by flow cytometry, and 5,000 OT-I cells were transferred intravenously into mice at the indicated time point before or after infection.

IFNγ blockade and sulfadiazine treatment

In vivo blockade of IFNγ signalling was performed by intraperitoneal injection of 200 µg per dose of rat IgG1 anti-IFNγ (clone XMG1.2, BioXcell) or IgG1 anti-horseradish peroxidase for control mice (HRPN, BioXcell). Injections were administered 2 times per week for 4 weeks before collection and analyses for parasite burden.

Where indicated, mice were treated with the anti-parasitic drug sulfadiazine (Sigma-Aldrich, S8626-25G) via drinking water. Sulfadiazine was reconstituted in dimethylsulfoxide to 50 mg ml^{-1} and added to drinking water at a final concentration of 0.25 mg ml^{-1}. Sulfadiazine-treated water was administered starting at 21 d.p.i. and refreshed every 3 days for 4 weeks.

Tissue processing and cell counting

To generate single-cell suspensions for flow cytometry, spleens were passed through a 40 µm filter, and red blood cells were lysed for 3 min at room temperature in ammonium-chloride-potassium (ACK) lysis buffer. Brains were diced into 1 mm pieces and digested at 37 °C and 5% CO_2 for 1.5 h with 250 µg ml^{-1} collagenase/dispase and 10 µg ml^{-1} DNase and then passed through a 70 µm filter. Leukocytes were then isolated through a 30% and 60% percoll gradient and density centrifugation at 900 *g* for 25 min. Whole blood was collected through submandibular bleed into 0.05 mM EDTA in PBS. Cells were pelleted, and red blood cells were lysed for 3 min at room temperature in ACK lysis buffer.

For quantification of cellularity and live leukocytes isolated from tissues, a fraction of processed cell suspensions was stained with Guava ViaCount Reagent (catalogue number 11-25209, 240 ml) and analysed on a Guava easyCyte flow cytometer according to manufacturer's protocol.

Generation of transgenic parasites

To generate Δ*bfd1* parasites, Pru-tub1-OVA-tdTomato parasites[68] were mechanically lysed from host cells by scraping and syringe releasing through a 27G needle. Parasites were pelleted for 10 min at 1,000 *g*, resuspended in Cytomix (10 mM KPO_4, 120 mM KCl, 150 mM $CaCl_2$, 5 mM $MgCl_2$, 25 mM HEPES, 2 mM EDTA) and combined with a DNA transfection mixture to a final volume of 400 µl. The final transfection mixture was supplemented with 2 mM ATP and 5 mM glutathione. Two guide RNAs contained on the Cas9-expressing pU6-Universal[93] (Addgene 52694) plasmid (Supplementary Data 1) were transfected to target the regions immediately upstream and downstream of the *BFD1* locus as previously described[12]. A pTUB-mNeonGreen repair template with homology arms matching the 40 bp regions flanking the cut sites was transfected to allow for sorting of Δ*bfd1* parasites by fluorescence-activated cell sorting (FACS). After sorting, parasites were plated at limiting dilutions to allow for screening of clonal parasites. A Δ*bfd1* clone was confirmed by PCR and sanger sequencing (Supplementary Data 1). However, despite these parasites being mNeonGreen positive, the mNeonGreen repair template was not found within the *BFD1* locus, indicating that this construct had randomly integrated into the parasite genome.

Generation of *bag1*-OVA parasites was performed by first generating the *pbag1OVA/sagCAT* plasmid (Supplementary Data 1) which contains (1) the *BAG1* promoter upstream of (2) the last 31 amino acids of the *T. gondii* major glycosyl-phosphatidylinositol-anchored surface antigen, P30, containing the signal sequence for targeting this protein to the parasitophorous vacuole, followed by (3) amino acids 140–386 of *ovalbumin* (OVA) and (4) a 3′ untranslated region of the *dihydrofolate reductase-thymidylate synthase* gene (3′dhfr). The OVA-3′dhfr fragment was subcloned in place of the red fluorescent protein (RFP)-3′dhfr fragment of the *pbag1RFP/sagCAT* plasmid[94] via BglII/NotI restriction digests. Transfections of type II Pruginaud (Pru) strain parasites were performed using electroporation, and stably expressing parasites were selected with chloramphenicol. Clonal parasite lines were generated by limiting dilution.

Immunohistochemistry

Brains were dissected by a sagittal cut along the midline, collected in 10% formalin, embedded in paraffin and sectioned. For identification of *T. gondii* parasites, slides were hydrated, and antigen was retrieved with 0.01 M sodium citrate buffer at pH 6.0, endogenous peroxidase was blocked with 0.3% H_2O_2, and sections were blocked with 2% goat serum. Parasites were detected with rabbit anti-*T. gondii* polyclonal antibody (gift from F. Araujo, Palo Alto Medical Foundation, 1:1,000) followed by biotinylated goat anti-rabbit IgG antibody (Vector Laboratories). Avidin-biotin complex (ABC) reagent and 3,3′-diaminobenzidine (DAB) substrate (Vector Laboratories) were used according to manufacturer's protocol to visualize parasite staining, and haematoxylin staining was

applied to visualize nuclei. Images were acquired with a Leica DM6000 Widefield Fluorescence Microscope using LAS X version 3.7.4.23463 software.

Pathological assessment

Brains were collected and processed for sectioning as described above. Haematoxylin and eosin (H&E)-stained sagittal sections of the brain, including the cerebral cortex and basal nuclei (Fig. 5 and Extended Data Fig. 5) or cerebral cortex and basal nuclei, hippocampus, thalamus, midbrain, cerebellum, pons and medulla (all other assessments) were assessed by a board-certified veterinary pathologist. The type of inflammatory cells and semiquantitative scores for the severity of parameters of interest (inflammation, haemorrhage, gliosis, necrosis and presence of parasites) were recorded for individual animals.

Flow cytometry

Single-cell suspensions were plated at up to 2×10^6 cells. Cells were Fc receptor blocked for 20 min with 0.5 µg ml^{-1} αCD16/32 (Clone 2.4G2) and 0.25% normal rat serum in FACs buffer (2% BSA and 0.02 mM EDTA in PBS) at 4 °C. If staining for tetramer, cells were then washed and incubated with 1:200 to 1:400 dilution of tetramer in FACs buffer at room temperature for 30 min. Following Fc blocking or tetramer stain, surface stain was applied, and cells were incubated for 30 min at 4 °C. Cells were then washed and resuspended in 0.1% paraformaldehyde in FACs buffer. If staining for intracellular antigens, cells were fixed and permeabilized with eBioscience Foxp3/Transcription Factor Staining Buffer Set according to manufacturer's protocol. Cells were then stained for intracellular antigens in permeabilization buffer for 30 min at 4 °C. Cells were washed and resuspended in FACs buffer. Stained cells were acquired on a BD LSR Fortessa, BD FACSymphony A5 or BD FACSymphony A3 using BD FACS DIVA v9.0 software. Analysis was performed with FlowJo v10.7.2. Gate placement was determined based on samples stained with all fluorescent antibodies used in the flow panel except the marker of interest. Gating strategies used to identify the populations analysed in these studies can be found in Extended Data Fig. 1d (OT-I T cells) and Supplementary Fig. 6 (CNS immune populations).

The following antibodies and reagents were used for staining: B220: BUV496, BD Biosciences: 612950, clone: RA3-6B2, RRID:AB_2870227, dilution 1:300; CD3: APC-ef780, Invitrogen: 47-0032-82, clone: 17A2, RRID:AB_1272181, dilution 1:300; CD3: BUV737, BD Biosciences: 612803, clone: 17A2, RRID:AB_2738781, dilution 1:300; CD3e: PE-cf594, BD Biosciences: 562286, clone: 145-2C11, RRID:AB_11153307, dilution 1:300; CD4: BUV496, BD Biosciences: 612952, clone: GK1.5, RRID:AB_2813886, dilution 1:200; CD4: BV650, Biolegend: 100555, clone: RM4-5, RRID:AB_2562529, dilution 1:400; CD4: FITC, eBioscience: 11-0041-85, clone: GK1.5, RRID:AB_464892, dilution 1:200; CD4: APC-ef780, Invitrogen: 47-0041-82, clone: GK1.5, RRID:AB_11218896, dilution 1:300; CD8a: BUV563, BD Biosciences: 748535, clone: 53-6.7, RRID:AB_2872946, dilution 1:200; CD8a: BUV615, BD Biosciences: 613004, clone: 53-6.7, RRID:AB_2870272, dilution 1:200; CD8a: BV650, Biolegend: 100742, clone: 53-6.7, RRID:AB_2563056, dilution 1:200; CD8b: APC-ef780, Invitrogen: 47-0083-82, clone: eBioH35-17.2, RRID:AB_2573943, dilution 1:200; CD11a: BUV805, BD Biosciences: 741919, clone: 2D7, RRID:AB_2871232, dilution 1:300; CD11b: BV650, Biolegend: 101259, clone: M1/70, RRID:AB_2566568, dilution 1:500; CD19: BUV395, BD Biosciences: 563557, clone: 1D3, RRID:AB_2722495, dilution 1:300; CD45: AF647, Biolegend: 103124, clone: 30-F11, RRID:AB_493533, dilution 1:200; CD45.1: ef450, Invitrogen: 48-0453-82, clone: A20, RRID:AB_1272189, dilution 1:200; CD45.1: BV711, Biolegend: 110739, clone: A20, RRID:AB_2562605, dilution 1:200; CD45.1: PE-Cy7, Biolegend: 110730, clone: A20, RRID:AB_1134168, dilution 1:200; CD45.2: APC, Biolegend: 109814, clone: 104, RRID:AB_389211, dilution 1:200; CD45.2: BV711, Biolegend: 109847, clone: 104, RRID:AB_2616859, dilution 1:200; CD69: BUV737, BD Biosciences: 612793, clone: H1.2F3, dilution 1:200; CD69: PerCP-Cy5.5, eBioscience: 45-0691-82, clone: H1.2F3, RRID:AB_1210703, dilution 1:400; CD103: PE, eBioscience: 12-1031-81, clone: 2E7, RRID:AB_11150242, dilution 1:200; CD103: BV605, Biolegend: 121433, clone: 2E7, RRID:AB_2629724, dilution 1:200; CD107a: PE-Cy7, Biolegend: 121620, clone: 1D4B, RRID:AB_2562146, dilution 1:300; CD127: BV421, Biolegend: 135027, clone: A7R34, RRID:AB_2563103, dilution 1:200; CTLA-4: APC-R700, BD Biosciences: 565778, clone: UC10-4F10-11, RRID:AB_2739350, dilution 1:200; CX3CR1: BV785, Biolegend: 149029, clone: SA011F11, RRID:AB_2565938, dilution 1:400; CX3CR1: PerCP-Cy5.5, Biolegend: 149009, clone: SA011F11, RRID:AB_2564493, dilution 1:400; F4/80: APC-ef780, eBiosciences: 47-4801-82, clone: BM8, RRID:AB_2735036, dilution 1:200; GFP: AF488, Biolegend: 338008, clone: FM264G, RRID:AB_2563288, dilution 1:300; H-2Kb: AF647, Biolegend: 116512, clone: AF6-88.5, RRID:AB_492917, dilution 1:200; I-A/I-E: AF700, Biolegend: 107622, clone: M5/144.15.2, RRID:AB_493727, dilution 1:300; I-A/I-E: BV711, Biolegend: 107643, clone: M5/144.15.2, RRID:AB_2565976, dilution 1:1200; IFNγ: BUV737, BD Biosciences: 612769, clone: XMG1.2, dilution 1:200; Ki-67: BV470, BD Biosciences: 566109, clone: B56, RRID:AB_2739511, dilution 1:200; KLRG1: BUV395, BD Biosciences: 740279, clone: 2F1, RRID:AB_2740018, dilution 1:200; Ly-6C: BV785, Biolegend: 128041, clone: HK1.4, RRID:AB_2565852, dilution 1:600; Ly-6G: BUV563, BD Biosciences: 612921, clone: 1A8, RRID:AB_2870206, dilution 1:400; NK1.1: BUV395, BD Biosciences: 564144, clone: PK136, RRID:AB_2738618, dilution 1:300; PD-1: BV421, Biolegend: 135221, clone: 29 F.1A12, RRID:AB_2562568, dilution 1:200; PD-1: BV605, Biolegend: 135220, clone: 29 F.1A12, RRID:AB_2562616, dilution 1:200; PD-1: BV785, Biolegend: 135225, clone: 29 F.1A12, RRID:AB_2563680, dilution 1:200; T-bet: AF647, Biolegend: 644804, clone: 4B10, RRID:AB_1595466, dilution 1:200; TCRβ: PerCP-Cy5.5, Biolegend: 109228, clone: H57-597, RRID:AB_1575173, dilution 1:500; TCRβ: ef450, Invitrogen: 48-5961-82, clone: H57-597, RRID:AB_11039532, dilution 1:200; Tetramer MHCI (OVA): PE, NIH Tetramer Core, peptide: SIINFEKL, dilution 1:300; Tetramer MHCI (Tgd057): APC, NIH Tetramer Core, peptide: SVLAFRRL, dilution 1:300; Tetramer MHCII (AS15): APC, NIH Tetramer Core, peptide: AVEIHRPVPGTAPPS, dilution 1:400; Tim3: BV605, Biolegend: 119721, clone: RMT3-23, RRID:AB_2616907, dilution 1:200; TNF: APC, Invitrogen: 17-7321-82, clone: MP6-XT22, RRID:AB_469508, dilution 1:200; Vα2 TCR: BUV615, BD Biosciences: 751416, clone: B20.1, RRID:AB_2875415, dilution 1:400; Vα2 TCR: PE, Biolegend: 127808, clone: B20.1, RRID:AB_1134183, dilution 1:300; Viability: GhostDye Violet 510, TONBO Biosciences: 13-0870-T100, dilution 1:300; Viability: GhostDye Red 780, TONBO Biosciences: 13-0865-T100, dilution 1:300.

T-cell peptide restimulation

Whole splenocytes or brain leukocytes were plated at a constant cell concentration. Cells were incubated with 1 µM SIINFEKL (OVA peptide), SVLAFRRL (Tgd057 peptide) or AVEIHRPVPGTAPPS (AS15 peptide) and fluorescently labelled αLAMP1 antibody for 2 h, followed by a further 2 h with Protein Transport Inhibitor Cocktail (Invitrogen: 00-4980-03). Cells were analysed for degranulation and cytokine production by fl ow cytometry.

Fluorescent imaging

Brains were collected from mice after cardiac perfusion with heparin (10 U ml^{-1}) in 0.9% saline followed by 4% paraformaldehyde, fixation in 4% paraformaldehyde for 24 h and cryoprotection at 4 °C in 30% sucrose for at least 24 h. Sagittal sections (40 µm) were cut on a freezing microtome and stored at 4 °C in cryoprotectant (0.05 M sodium phosphate buffer with 30% glycerol and 30% ethylene glycol). Staining and imaging for neurons, astrocytes, dolichos biflorus lectin and OVA in infected brains was performed using the following reagents and antibodies: anti-OVA, Abcam: ab181688, dilution 1:200; DBA, Vector laboratories: B1035, dilution 1:500; anti-GFAP, DAKO: Z0334, dilution 1:200; anti-MAP2, Abcam: ab5392, dilution 1:2,000; anti-NeuN, Millipore: MAB3778, dilution 1:200; anti-Neurofilament, Abcam: ab4680,

dilution 1:20,000. Anti-SAG1 (DG52), dilution 1:500 and SRS9, dilution 1:2,000 antibodies were gifted by J. Boothroyd[95,96]. Stained sections were mounted on slides using ProLong Diamond Anti-Fade Mountant with DAPI (Invitrogen P36962) according to manufacturer's protocol. Images were acquired on a Zeiss LSM 880 inverted confocal microscope (University of Arizona, Imaging Core) and Nikon E600 upright widefield microscope (University of Pennsylvania, Penn Vet Imaging Core); images were analysed using Zen 2.6 blue edition software and counted using ImageJ version 1.53 v software.

For quantification of cyst size in WT and *Stat1*$^{\Delta NEU}$ mice, perfused brains were frozen in Optimal Cutting Temperature Compound (Fisher Scientific, catalogue number 23-730-571), and 10 µm sections were cut on a vibratome. Sections were mounted with ProLong Diamond Anti-Fade Mountant with DAPI. Sections were imaged on a Leica SP5-II at ×60 magnification. Cysts were defined as vacuoles with >32 parasites present. Cyst area was quantified using Imaris (v9.7.2) microscopy imaging software, and images were generated with LAS AF (v2.7.3.9723) software. Five to 20 vacuoles per brain were quantified.

Imaging of bag1-OVA parasites in vitro was performed using HFFs cultured on eight-well chamber slides. Cells were infected at multiplicity of infection (MOI) = 3 for 3 h. Stress-induced cyst formation was performed by culturing infected cells under cyst-inducing conditions for 4 days: cells were incubated without supplemental CO_2 in RPMI media (pH 8.0) without sodium bicarbonate, supplemented with 1% FBS, 10 mg ml^{-1} HEPES, 100 U ml^{-1} penicillin and 100 µg ml^{-1} streptomycin. Media was replaced every 48 h (ref. 64). Cells were then stained with anti-OVA (Abcam ab181688) and DAPI nuclear stain. Slides were imaged on a Nikon E600 upright widefield microscope (University of Pennsylvania Imaging Core).

Quantification of serum IFNγ

Blood was collected by submandibular bleed and clotted at room temperature for 1 h. Serum was separated through centrifugation for 10 min at 14,000 *g*. Serum was diluted between 1:5 and 1:20, and IFNγ levels were assayed by BD Mouse IFNγ Flex Set Cytometric Bead Array according to manufacturer's protocol. Beads were analysed by flow cytometry on a BD Canto.

Quantification of parasite burden by quantitative PCR

Sagittal sections of brain tissue were snap frozen and stored at −20 °C. DNA was isolated using QIAGEN DNeasy Blood and Tissue Kit according to manufacturer's protocol. DNA quality and concentration was assessed on a Nanodrop ND-1000 UV–Vis Spectrophotometer. About 200 ng of DNA was used to quantify parasite burden by quantitative PCR (qPCR) with Power SYBR Green Master Mix and primers specific for the *T. gondii* B1 gene (Supplementary Data 1). qPCR was performed on Applied Biosystems ViiA7 with the following conditions: hold phase for 2 min at 50 °C and 10 min at 95 °C; PCR phase (occurs 50 times) for 15 s at 95 °C and 1 min at 60 °C.

Statistical information

Statistical tests were run in Prism software version 10.2.3 (Graphpad). Data were analysed by two-sided Student's *t*-tests, two-sided Student's *t*-tests with Bonferroni–Dunn correction for multiple tests, two-way analysis of variance (ANOVA) or two-sided Mann–Whitney tests where indicated. Not significant, $P \geq 0.05$; *$P < 0.05$; **$P < 0.01$; ***$P < 0.001$; ****$P < 0.0001$. Precise *P* values for significant trends are included in the corresponding figure legends.

Reporting summary

Further information on research design is available in the Nature Portfolio Reporting Summary linked to this article.

Data availability

Source data are provided with this paper.

Code availability

All code relating to the generation of ODEs are available on GitHub using the link provided: https://github.com/acwinn/TGondii.

References

1. Munz, C. Latency and lytic replication in Epstein–Barr virus-associated oncogenesis. *Nat. Rev. Microbiol.* **17**, 691–700 (2019).
2. Singh, N. & Tscharke, D. C. Herpes simplex virus latency is noisier the closer we look. *J. Virol.* **94** https://doi.org/10.1128/JVI.01701-19 (2020).
3. Alanio, A. Dormancy in *Cryptococcus neoformans*: 60 years of accumulating evidence. *J. Clin. Invest.* **130**, 3353–3360 (2020).
4. Zhao, X. Y. & Ewald, S. E. The molecular biology and immune control of chronic *Toxoplasma gondii* infection. *J. Clin. Invest.* **130**, 3370–3380 (2020).
5. Goodrum, F. Human cytomegalovirus latency: approaching the Gordian knot. *Annu. Rev. Virol.* **3**, 333–357 (2016).
6. Schäfer, C., Zanghi, G., Vaughan, A. M. & Kappe, S. H. I. *Plasmodium vivax* latent liver stage infection and relapse: biological insights and new experimental tools. *Ann. Rev. Microbiol.* **75**, 87–106 (2021).
7. Pirofski, L.-A. & Casadevall, A. The state of latency in microbial pathogenesis. *J. Clin. Invest.* **130**, 4525–4531 (2020).
8. Mackowiak, P. A. Microbial latency. *Rev. Infect. Dis.* **6**, 649–668 (1984).
9. Sokol-Borrelli, S. L., Coombs, R. S. & Boyle, J. P. A comparison of stage conversion in the coccidian apicomplexans *Toxoplasma gondii*, *Hammondia hammondi*, and *Neospora caninum*. *Front. Cell. Infect. Microbiol.* **10**, 608283 (2020).
10. Matta, S. K., Rinkenberger, N., Dunay, I. R. & Sibley, L. D. *Toxoplasma gondii* infection and its implications within the central nervous system. *Nat. Rev. Microbiol.* **19**, 467–480 (2021).
11. Cerutti, A., Blanchard, N. & Besteiro, S. The bradyzoite: a key developmental stage for the persistence and pathogenesis of toxoplasmosis. *Pathogens* **9** https://doi.org/10.3390/pathogens9030234 (2020).
12. Waldman, B. S. et al. Identification of a master regulator of differentiation in *Toxoplasma*. *Cell* **180**, 359–372.e316 (2020).
13. Licon, M. H. et al. A positive feedback loop controls *Toxoplasma* chronic differentiation. *Nat. Microbiol.* **8**, 889–904 (2023).
14. Sokol-Borrelli, S. L. et al. A transcriptional network required for bradyzoite development in *Toxoplasma gondii* is dispensable for recrudescent disease. *Nat. Commun.* **14**, 6078 (2023).
15. Su, C. et al. Recent expansion of *Toxoplasma* through enhanced oral transmission. *Science* **299**, 414–416 (2003).
16. Coombes, J. L. & Robey, E. A. Dynamic imaging of host–pathogen interactions in vivo. *Nat. Rev. Immunol.* **10**, 353–364 (2010).
17. John, B., Weninger, W. & Hunter, C. A. Advances in imaging the innate and adaptive immune response to *Toxoplasma gondii*. *Future Microbiol.* **5**, 1321–1328 (2010).
18. Watts, E. et al. Novel approaches reveal that *Toxoplasma gondii* bradyzoites within tissue cysts are dynamic and replicating entities in vivo. *mBio* **6**, e01155–01115 (2015).
19. Tomita, T. et al. *Toxoplasma gondii* matrix antigen 1 is a secreted immunomodulatory effector. *mBio* **12** https://doi.org/10.1128/mBio.00603-21 (2021).
20. Mayoral, J., Shamamian, P. & Weiss, L. M. In vitro characterization of protein effector export in the bradyzoite stage of *Toxoplasma gondii*. *mBio* **11** https://doi.org/10.1128/mBio.00046-20 (2020).
21. Burke, J. M., Roberts, C. W., Hunter, C. A., Murray, M. & Alexander, J. Temporal differences in the expression of mRNA for IL-10 and IFN-gamma in the brains and spleens of C57BL/10 mice infected with *Toxoplasma gondii*. *Parasite Immunol.* **16**, 305–314 (1994).

22. Young, J. D. & McGwire, B. S. Infliximab and reactivation of cerebral toxoplasmosis. *N. Engl. J. Med.* **353**, 1530–1531 (2005).
23. Luft, B. J. & Remington, J. S. Toxoplasmic encephalitis. *J. Infect. Dis.* **157**, 1–6 (1988).
24. Gazzinelli, R. T. et al. In the absence of endogenous IL-10, mice acutely infected with *Toxoplasma gondii* succumb to a lethal immune response dependent on $CD4^+$ T cells and accompanied by overproduction of IL-12, IFN-gamma and TNF-alpha. *J. Immunol.* **157**, 798–805 (1996).
25. Villarino, A. et al. The IL-27R (WSX-1) is required to suppress T cell hyperactivity during infection. *Immunity* **19**, 645–655 (2003).
26. Wilson, E. H., Wille-Reece, U., Dzierszinski, F. & Hunter, C. A. A critical role for IL-10 in limiting inflammation during toxoplasmic encephalitis. *J. Neuroimmunol.* **165**, 63–74 (2005).
27. Deckert-Schluter, M. et al. Interleukin-10 downregulates the intracerebral immune response in chronic *Toxoplasma* encephalitis. *J. Neuroimmunol.* **76**, 167–176 (1997).
28. Stumhofer, J. S. et al. Interleukin 27 negatively regulates the development of interleukin 17-producing T helper cells during chronic inflammation of the central nervous system. *Nat. Immunol.* **7**, 937–945 (2006).
29. Aliberti, J. Host persistence: exploitation of anti-inflammatory pathways by *Toxoplasma gondii*. *Nat. Rev. Immunol.* **5**, 162–170 (2005).
30. Buckley, M. W. & McGavern, D. B. Immune dynamics in the CNS and its barriers during homeostasis and disease. *Immunol. Rev.* **306**, 58–75 (2022).
31. Klein, R. S. & Hunter, C. A. Protective and pathological immunity during central nervous system infections. *Immunity* **46**, 891–909 (2017).
32. Miller, K. D., Schnell, M. J. & Rall, G. F. Keeping it in check: chronic viral infection and antiviral immunity in the brain. *Nat. Rev. Neurosci.* **17**, 766–776 (2016).
33. Rose, R. W., Vorobyeva, A. G., Skipworth, J. D., Nicolas, E. & Rall, G. F. Altered levels of STAT1 and STAT3 influence the neuronal response to interferon gamma. *J. Neuroimmunol.* **192**, 145–156 (2007).
34. Chandrasekaran, S. et al. IFN-gamma stimulated murine and human neurons mount anti-parasitic defenses against the intracellular parasite *Toxoplasma gondii*. *Nat. Commun.* **13**, 4605 (2022).
35. Chevalier, G. et al. Neurons are MHC class I-dependent targets for CD8 T cells upon neurotropic viral infection. *PLoS Pathog.* **7**, e1002393 (2011).
36. Moseman, E. A., Blanchard, A. C., Nayak, D. & McGavern, D. B. T cell engagement of cross-presenting microglia protects the brain from a nasal virus infection. *Sci. Immunol.* **5** https://doi.org/10.1126/sciimmunol.abb1817 (2020).
37. Binder, G. K. & Griffin, D. E. Interferon-gamma-mediated site-specific clearance of alphavirus from CNS neurons. *Science* **293**, 303–306 (2001).
38. Patterson, C. E., Lawrence, D. M., Echols, L. A. & Rall, G. F. Immune-mediated protection from measles virus-induced central nervous system disease is noncytolytic and gamma interferon dependent. *J. Virol.* **76**, 4497–4506 (2002).
39. Burdeinick-Kerr, R., Govindarajan, D. & Griffin, D. E. Noncytolytic clearance of sindbis virus infection from neurons by gamma interferon is dependent on Jak/STAT signaling. *J. Virol.* **83**, 3429–3435 (2009).
40. Schluter, D., Deckert, M., Hof, H. & Frei, K. *Toxoplasma gondii* infection of neurons induces neuronal cytokine and chemokine production, but gamma interferon- and tumor necrosis factor-stimulated neurons fail to inhibit the invasion and growth of *T. gondii*. *Infect. Immun.* **69**, 7889–7893 (2001).
41. Suzuki, Y., Orellana, M. A., Schreiber, R. D. & Remington, J. S. Interferon-gamma: the major mediator of resistance against *Toxoplasma gondii*. *Science* **240**, 516–518 (1988).
42. Salvioni, A. et al. Robust control of a brain-persisting parasite through MHC I presentation by infected neurons. *Cell Rep.* **27**, 3254–3268 e3258 (2019).
43. Porte, R. et al. Protective function and differentiation cues of brain-resident $CD8^+$ T cells during surveillance of latent *Toxoplasma gondii* infection. *Proc. Natl Acad. Sci. USA* **121**, e2403054121 (2024).
44. Denkers, E. Y. et al. Perforin-mediated cytolysis plays a limited role in host resistance to *Toxoplasma gondii*. *J. Immunol.* **159**, 1903–1908 (1997).
45. Suzuki, Y. et al. Removal of *Toxoplasma gondii* cysts from the brain by perforin-mediated activity of $CD8^+$ T cells. *Am. J. Pathol.* **176**, 1607–1613 (2010).
46. Wilson, E. H. et al. Behavior of parasite-specific effector $CD8^+$ T cells in the brain and visualization of a kinesis-associated system of reticular fibers. *Immunity* **30**, 300–311 (2009).
47. Schaeffer, M. et al. Dynamic imaging of T cell–parasite interactions in the brains of mice chronically infected with *Toxoplasma gondii*. *J. Immunol.* **182**, 6379–6393 (2009).
48. Shallberg, L. A. et al. Impact of secondary TCR engagement on the heterogeneity of pathogen-specific $CD8^+$ T cell response during acute and chronic toxoplasmosis. *PLoS Pathog.* **18**, e1010296 (2022).
49. John, B. et al. Analysis of behavior and trafficking of dendritic cells within the brain during toxoplasmic encephalitis. *PLoS Pathog.* **7**, e1002246 (2011).
50. Tiwari, A. et al. Penetration of CD8(+) cytotoxic T cells into large target, tissue cysts of *Toxoplasma gondii*, leads to its elimination. *Am. J. Pathol.* **189**, 1594–1607 (2019).
51. Fischer, H. G., Bonifas, U. & Reichmann, G. Phenotype and functions of brain dendritic cells emerging during chronic infection of mice with *Toxoplasma gondii*. *J. Immunol.* **164**, 4826–4834 (2000).
52. Kim, S. K., Karasov, A. & Boothroyd, J. C. Bradyzoite-specific surface antigen SRS9 plays a role in maintaining *Toxoplasma gondii* persistence in the brain and in host control of parasite replication in the intestine. *Infect. Immun.* **75**, 1626–1634 (2007).
53. Sullivan, A. et al. A mathematical model for within-host *Toxoplasma gondii* invasion dynamics. *Math. Biosci. Eng.* **9**, 647–662 (2012).
54. Sullivan, A. M. et al. Evidence for finely-regulated asynchronous growth of *Toxoplasma gondii* cysts based on data-driven model selection. *PLoS Comput. Biol.* **9**, e1003283 (2013).
55. Harris, T. H. et al. Generalized Levy walks and the role of chemokines in migration of effector $CD8^+$ T cells. *Nature* **486**, 545–548 (2012).
56. Christian, D. A. et al. cDC1 coordinate innate and adaptive responses in the omentum required for T cell priming and memory. *Sci. Immunol.* **7**, eabq7432 (2022).
57. Kafsack, B. F., Carruthers, V. B. & Pineda, F. J. Kinetic modeling of *Toxoplasma gondii* invasion. *J. Theor. Biol.* **249**, 817–825 (2007).
58. Radke, J. R. et al. Defining the cell cycle for the tachyzoite stage of *Toxoplasma gondii*. *Mol. Biochem. Parasitol.* **115**, 165–175 (2001).
59. Black, M. W. & Boothroyd, J. C. Lytic cycle of *Toxoplasma gondii*. *Microbiol. Mol. Biol. Rev.* **64**, 607–623 (2000).
60. Jerome, M. E., Radke, J. R., Bohne, W., Roos, D. S. & White, M. W. *Toxoplasma gondii* bradyzoites form spontaneously during sporozoite-initiated development. *Infect. Immun.* **66**, 4838–4844 (1998).
61. Lieberman, L. A., Banica, M., Reiner, S. L. & Hunter, C. A. STAT1 plays a critical role in the regulation of antimicrobial effector mechanisms, but not in the development of Th1-type responses during toxoplasmosis. *J. Immunol.* **172**, 457–463 (2004).

62. Channon, J. Y., Seguin, R. M. & Kasper, L. H. Differential infectivity and division of *Toxoplasma gondii* in human peripheral blood leukocytes. *Infect. Immun.* **68**, 4822–4826 (2000).
63. Tanaka, N., Ashour, D., Dratz, E. & Halonen, S. Use of human induced pluripotent stem cell-derived neurons as a model for cerebral toxoplasmosis. *Microbes Infect.* **18**, 496–504 (2016).
64. Kochanowsky, J. A., Chandrasekaran, S., Sanchez, J. R., Thomas, K. K. & Koshy, A. A. ROP16-mediated activation of STAT6 enhances cyst development of type III *Toxoplasma gondii* in neurons. *PLoS Pathog.* **19**, e1011347 (2023).
65. Ferguson, D. J., Hutchison, W. M. & Pettersen, E. Tissue cyst rupture in mice chronically infected with *Toxoplasma gondii*. An immunocytochemical and ultrastructural study. *Parasitol. Res.* **75**, 599–603 (1989).
66. Ahmed, R. & Gray, D. Immunological memory and protective immunity: understanding their relation. *Science* **272**, 54–60 (1996).
67. Harty, J. T. & Badovinac, V. P. Influence of effector molecules on the CD8(+) T cell response to infection. *Curr. Opin. Immunol.* **14**, 360–365 (2002).
68. Pepper, M., Dzierszinski, F., Crawford, A., Hunter, C. A. & Roos, D. Development of a system to study $CD4^+$-T-cell responses to transgenic ovalbumin-expressing *Toxoplasma gondii* during toxoplasmosis. *Infect. Immun.* **72**, 7240–7246 (2004).
69. Yap, G. S. & Sher, A. Effector cells of both nonhemopoietic and hemopoietic origin are required for interferon (IFN)-γ– and tumor necrosis factor (TNF)-α–dependent host resistance to the intracellular pathogen, *Toxoplasma gondii*. *J. Exp. Med.* **189**, 1083–1092 (1999).
70. Cowan, M. N. et al. Microglial STAT1-sufficiency is required for resistance to toxoplasmic encephalitis. *PLoS Pathog.* **18**, e1010637 (2022).
71. Hidano, S. et al. STAT1 signaling in astrocytes is essential for control of infection in the central nervous system. *mBio* **7** https://doi.org/10.1128/mBio.01881-16 (2016).
72. Suzuki, Y., Joh, K., Orellana, M. A., Conley, F. K. & Remington, J. S. A gene(s) within the H-2D region determines the development of toxoplasmic encephalitis in mice. *Immunology* **74**, 732–739 (1991).
73. Bergersen, K. V., Barnes, A., Worth, D., David, C. & Wilson, E. H. Targeted transcriptomic analysis of C57BL/6 and BALB/c mice during progressive chronic *Toxoplasma gondii* infection reveals changes in host and parasite gene expression relating to neuropathology and resolution. *Front. Cell Infect. Microbiol.* **11**, 645778 (2021).
74. Rall, G. F., Mucke, L. & Oldstone, M. B. Consequences of cytotoxic T lymphocyte interaction with major histocompatibility complex class I-expressing neurons in vivo. *J. Exp. Med.* **182**, 1201–1212 (1995).
75. Gazzinelli, R., Xu, Y., Hieny, S., Cheever, A. & Sher, A. Simultaneous depletion of $CD4^+$ and $CD8^+$ T lymphocytes is required to reactivate chronic infection with *Toxoplasma gondii*. *J. Immunol.* **149**, 175–180 (1992).
76. Kwok, L. Y. et al. The induction and kinetics of antigen-specific CD8 T cells are defined by the stage specificity and compartmentalization of the antigen in murine toxoplasmosis. *J. Immunol.* **170**, 1949–1957 (2003).
77. Herz, J., Johnson, K. R. & McGavern, D. B. Therapeutic antiviral T cells noncytopathically clear persistently infected microglia after conversion into antigen-presenting cells. *J. Exp. Med.* **212**, 1153–1169 (2015).
78. Cabral, C. M. et al. Neurons are the primary target cell for the brain-tropic intracellular parasite *Toxoplasma gondii*. *PLoS Pathog.* **12**, e1005447 (2016).
79. Frickel, E. M. & Hunter, C. A. Lessons from *Toxoplasma*: host responses that mediate parasite control and the microbial effectors that subvert them. *J. Exp. Med.* **218** https://doi.org/10.1084/jem.20201314 (2021).
80. Gay, G. A.-O. et al. *Toxoplasma gondii* TgIST co-opts host chromatin repressors dampening STAT1-dependent gene regulation and IFN-γ-mediated host defenses. *J. Exp. Med.* **213**, 1779–1798 (2016).
81. Seizova, S. et al. Transcriptional modification of host cells harboring *Toxoplasma gondii* bradyzoites prevents IFN gamma-mediated cell death. *Cell Host Microbe* **30**, 232–247.e236 (2022).
82. Olias, P., Etheridge, R. D., Zhang, Y., Holtzman, M. J. & Sibley, L. D. *Toxoplasma* effector recruits the Mi-2/NuRD complex to repress STAT1 transcription and block IFN-γ-dependent gene expression. *Cell Host Microbe* **20**, 72–82 (2016).
83. Landrith, T. A. et al. CD103(+) CD8 T cells in the *Toxoplasma*-infected brain exhibit a tissue-resident memory transcriptional profile. *Front. Immunol.* **8**, 335 (2017).
84. Bhadra, R., Gigley, J. P., Weiss, L. M. & Khan, I. A. Control of Toxoplasma reactivation by rescue of dysfunctional CD8+ T-cell response via PD-1-PDL-1 blockade. *Proc. Natl Acad. Sci.* **102**, 9196–9201 (2011).
85. Chauhan, P. & Lokensgard, J. R. Glial cell expression of PD-L1. *Int. J. Mol. Sci.* **20** https://doi.org/10.3390/ijms20071677 (2019).
86. Meerschaert, K. A. et al. Neuronally expressed PDL1, not PD1, suppresses acute nociception. *Brain Behav. Immun.* **106**, 233–246 (2022).
87. Handel, A., La Gruta, N. L. & Thomas, P. G. Simulation modelling for immunologists. *Nat. Rev. Immunol.* **20**, 186–195 (2020).
88. Kirschner, D., Pienaar, E., Marino, S. & Linderman, J. J. A review of computational and mathematical modeling contributions to our understanding of *Mycobacterium tuberculosis* within-host infection and treatment. *Curr. Opin. Syst. Biol.* **3**, 170–185 (2017).
89. Yap, G. S. Avirulence: an essential feature of the parasitic lifestyle. *Trends Parasitol.* **38**, 1028–1030 (2022).
90. Matthews, K. R., McCulloch, R. & Morrison, L. J. The within-host dynamics of African trypanosome infections. *Philos. Trans. R. Soc. Lond. B* **370** https://doi.org/10.1098/rstb.2014.0288 (2015).
91. Brunet, L. R., Finkelman, F. D., Cheever, A. W., Kopf, M. A. & Pearce, E. J. IL-4 protects against TNF-a-mediated cachexia and death during acute Schistosomiasis. *J. Immunol.* **159**, 777–785 (1997).
92. Klover, P. J. et al. Loss of STAT1 from mouse mammary epithelium results in an increased Neu-induced tumor burden. *Neoplasia* **12**, 899–905 (2010).
93. Sidik, S. M., Hackett, C. G., Tran, F., Westwood, N. J. & Lourido, S. Efficient genome engineering of *Toxoplasma gondii* using CRISPR/Cas9. *PLoS ONE* **9**, e100450 (2014).
94. Dzierszinski, F., Nishi, M., Ouko, L. & Roos, D. S. Dynamics of *Toxoplasma gondii* differentiation. *Eukaryot. Cell* **3**, 992–1003 (2004).
95. Burg, J. L., Perelman, D., Kasper, L. H., Ware, P. L. & Boothroyd, J. C. Molecular analysis of the gene encoding the major surface antigen of *Toxoplasma gondii*. *J. Immunol.* **141**, 3584–3591 (1988).
96. Kim, S. K. & Boothroyd, J. C. Stage-specific expression of surface antigens by *Toxoplasma gondii* as a mechanism to facilitate parasite persistence. *J. Immunol.* **174**, 8038–8048 (2005).

Acknowledgements

We thank A. T. Phan for contributions and assistance with experiments. We also thank G. Ruthel and the Penn Vet Imaging Core for kindly providing microscopy equipment, assistance with image acquisition and access to imaging analysis software. These studies were supported by funding from the National Institutes of Health, R01 AI157247 (C.A.H. and A.A.K.); National Institute of Allergy and Infectious Diseases, U01 AI160664 (D.A.C.), F31 AI161962 (D.L.A.), T32 CA009140 (M.E.B.) and R01 AI158501 (S.L.); and Institutional funding from the College of Medicine and BIO5 Institute of the University of Arizona (A.A.K.).

Author contributions

Conceptualization: L.A.S., C.A.H., A.A.K. and S.L. Methodology: L.A.S., A.W., J.N.E., S.C., C.J.G., E.F.M. and F.D. Investigation: L.A.S., J.N.E., A.W.,

S.C., C.J.G., E.F.M., E.W., C.K., D.A.C., D.L.A., M.E.B. and M.J. Funding acquisition: L.A.S., C.A.H., A.A.K., S.L. and E.K. Supervision: L.A.S., C.A.H., A.A.K., S.L., F.D. and E.K. Writing—original draft: L.A.S. and C.A.H. Writing—review and editing: J.N.E., C.A.H., A.W., A.A.K., S.L., S.C., E.W., D.A.C., M.E.B. and L.A.S.

Competing interests
The authors declare no competing interests.

Additional information
Extended data is available for this paper at https://doi.org/10.1038/s41564-025-01967-z.

Supplementary information The online version contains supplementary material available at https://doi.org/10.1038/s41564-025-01967-z.

Correspondence and requests for materials should be addressed to Christopher A. Hunter.

Peer review information *Nature Microbiology* thanks Jason Gigley and the other, anonymous, reviewer(s) for their contribution to the peer review of this work.

[1]Department of Pathobiology, School of Veterinary Medicine, University of Pennsylvania, Philadelphia, PA, USA. [2]Department of Physics and Astronomy, School of Arts and Sciences, University of Pennsylvania, Philadelphia, PA, USA. [3]BIO5 Institute, University of Arizona, Tucson, AZ, USA. [4]Whitehead Institute for Biomedical Research, Cambridge, MA, USA. [5]Department of Biology, Massachusetts Institute of Technology, Cambridge, MA, USA. [6]Department of Immunology, University of Arizona, Tucson, AZ, USA. [7]Comparative Pathology Core, Department of Pathobiology, School of Veterinary Medicine, University of Pennsylvania, Philadelphia, PA, USA. [8]Department of Comparative Pathobiology, Purdue University College of Veterinary Medicine, West Lafayette, IN, USA. [9]The Royal Ottawa Mental Health Center, Institute of Mental Health Research, Ottawa, Ontario, Canada. [10]Center for Computational Biology, Flatiron Institute, New York, NY, USA. [11]Department of Neurology, University of Arizona, Tucson, AZ, USA. [12]These authors contributed equally: Julia N. Eberhard, Lindsey A. Shallberg, Aaron Winn. ✉e-mail: chunter@vet.upenn.edu

https://doi.org/10.1038/s41564-025-01967-z

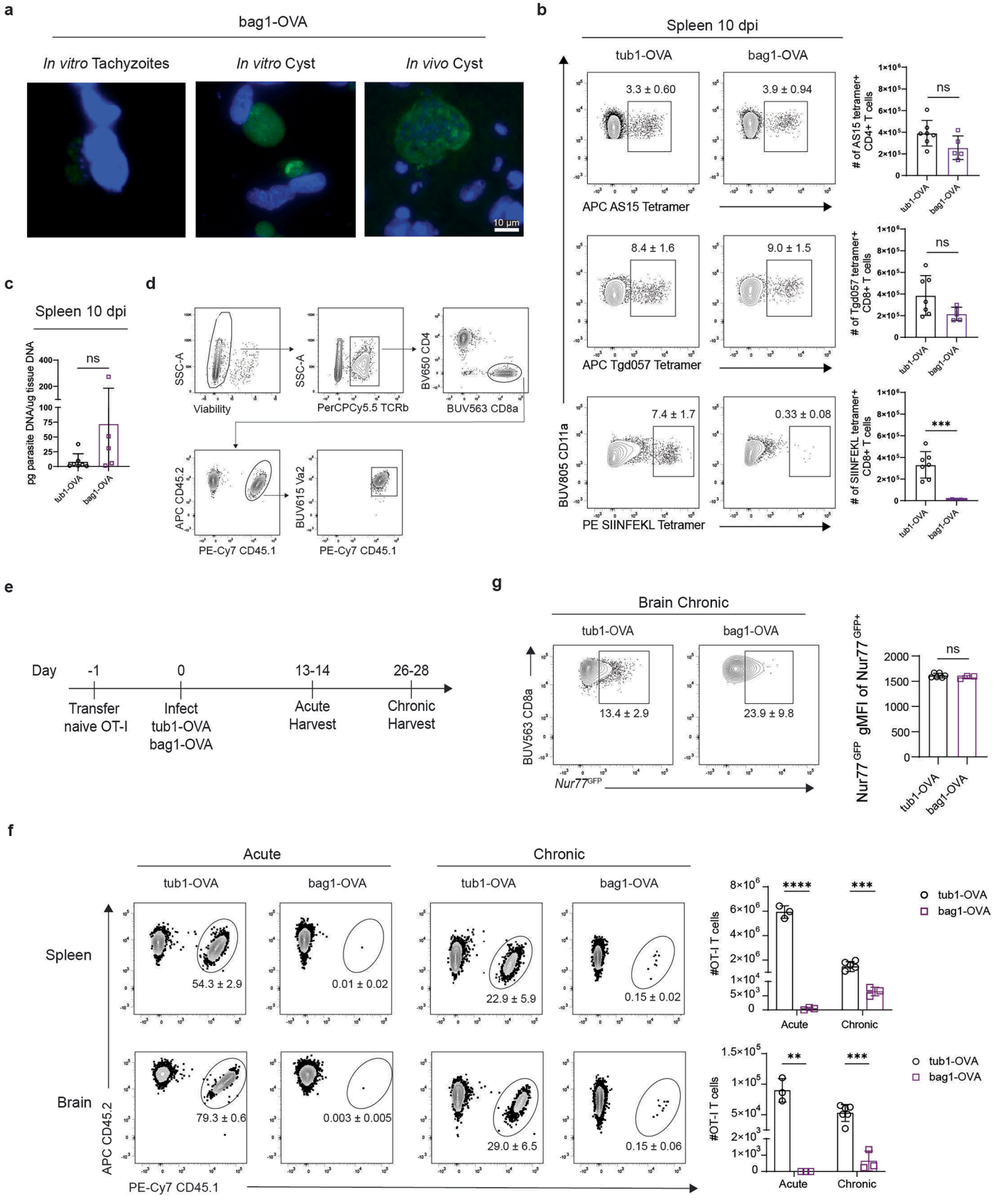

Extended Data Fig. 1 | See next page for caption.

https://doi.org/10.1038/s41564-025-01967-z

Extended Data Fig. 1 | Virulence and T cell responses during early stages of tub1-OVA and bag1-OVA infection. a, Representative images of *in vitro* bag1-OVA tachyzoite- or cyst-infected HFFs, and *in vivo* bag1-OVA tissue cysts in the brains of mice at 30 dpi. Samples were stained with DAPI nuclear stain and anti-OVA antibody. DAPI (blue); OVA (green). Scale bar = 10 µm. **b-c**, C57BL/6 J mice were infected with tub1-OVA (n = 7 mice) or bag1-OVA (n = 5 mice) parasites, and spleens were harvested and analyzed at 10 dpi. **b**, Frequency and number of *T. gondii* peptide and SIINFEKL tetramer$^+$ CD4$^+$ and CD8$^+$ T cells (***p = 0002.) **c**, Quantification of parasite burden by qPCR. **d**, Gating strategy for identifying OT-I T cells by flow cytometry. Cells were pre-gated on single cells. **e**, Experimental design for **f-g**. Naive CD45.1$^+$CD45.2$^+$ Nur77^{GFP} OT-I T cells were transferred 1 day prior to infection with tub1-OVA or bag1-OVA parasites. Spleens and brains were harvested from infected mice and analyzed by flow cytometry during acute (n = 3 mice/group) and chronic (tub1-OVA, n = 5 mice; bag1-OVA, n = 3 mice) infection. **f**, Frequency and number of OT-I T cells (spleen: ****p = 0.000036, ***p = 0.000535; brain: **p = 0.001260, ***p = 0.000411.) **g**, Frequency and gMFI of Nur77^{GFP} expression in brain OT-I T cells during chronic infection (tub1-OVA, n = 5 mice; bag1-OVA, n = 3 mice.) Data are representative of 2 independent experiments. Data analyzed by two-sided unpaired Student's *t*-test; ns $p > 0.05$. Bar graphs depict the mean ± SD.

https://doi.org/10.1038/s41564-025-01967-z

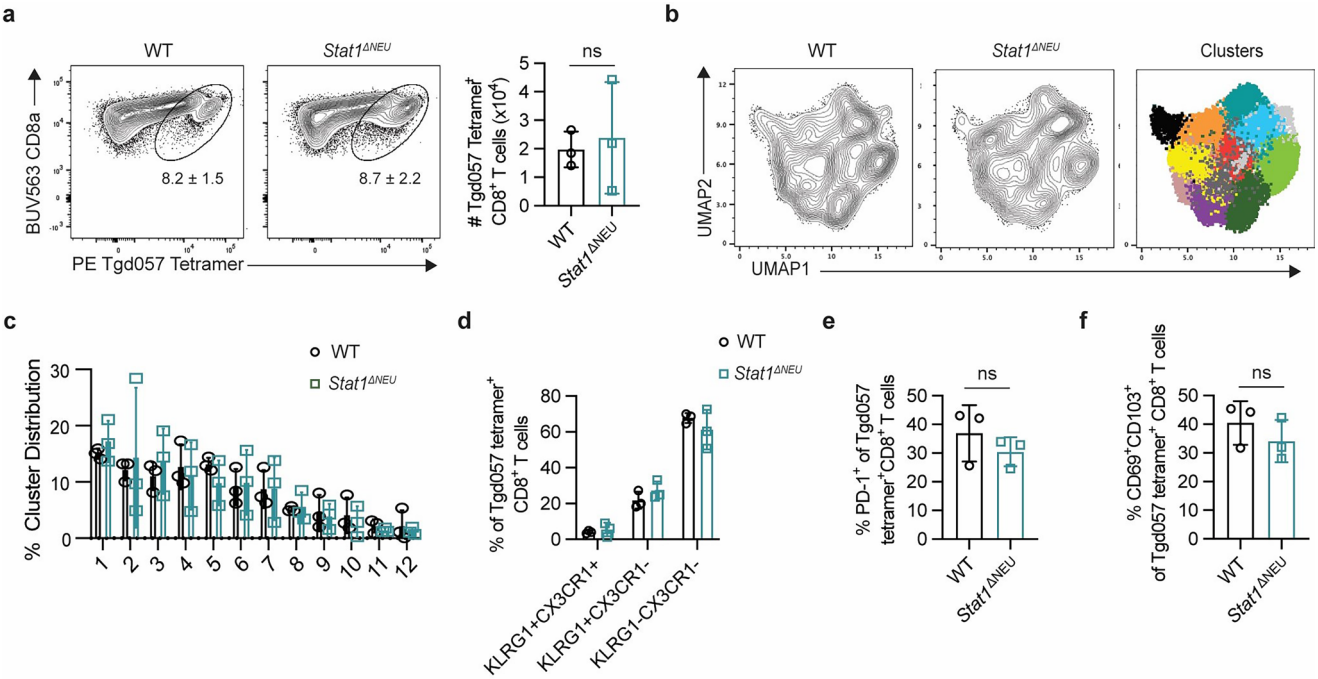

Extended Data Fig. 2 | Similar *T. gondii* specific T cell responses are induced in the brains of WT and *Stat1*$^{\Delta NEU}$ mice at 3 months post-infection. Brains from C57BL/6 J (WT) and *Stat1*$^{\Delta NEU}$ mice infected with *T. gondii* were harvested at 3 mpi (n = 3 mice/group.) *T. gondii*-specific T cells were quantified and phenotyping was performed by flow cytometry. **a**, Frequency and number of *T. gondii* tetramer$^+$ CD8$^+$ T cells. **b**, UMAP and X-shift unsupervised clustering analysis of tetramer$^+$ T cells. Colors represent 12 individual clusters. **c**, Distribution of tetramer$^+$ T cells across the clusters identified in **b**. **d**-**f**, Phenotyping of tetramer$^+$ CD8$^+$ T cells by flow cytometry. Data are representative of 2 independent experiments. Data analyzed by two-sided unpaired Student's *t*-test; Bonferroni-Dunn correction for multiple comparisons was included in statistical analyses performed in **c** and **d**; ns $p > 0.05$. Bar graphs depict the mean ± SD.

https://doi.org/10.1038/s41564-025-01967-z

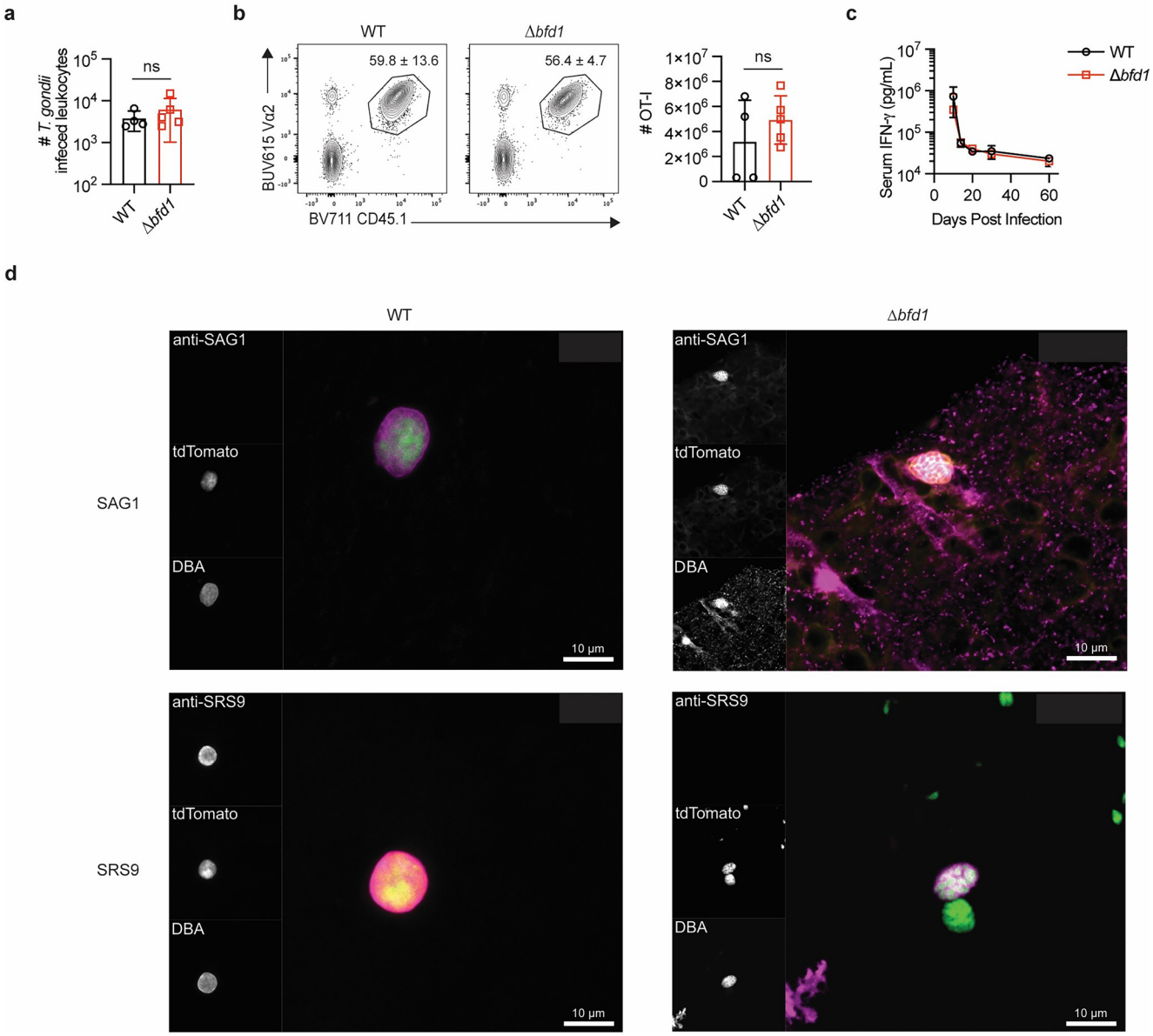

Extended Data Fig. 3 | WT and *Δbfd1* parasites induce comparable immune responses during acute infection. a-b, C57BL/6 J mice were infected with tdTomato$^+$ WT (n = 4 mice) or *Δbfd1* (n = 5 mice) parasites, and spleens were harvested and analyzed at 14 dpi. Naive CD45.1$^+$CD45.2$^+$ OT-I T cells were transferred one day prior to infection. **a**, Quantification of *T. gondii*-infected cells in the spleen by flow cytometry **b**, Splenic OT-I T cell frequency and numbers. **c**, Quantification of serum IFN-γ levels during WT (n = 4 mice) or *Δbfd1* (n = 5 mice) infection. **d**, Representative images of *T. gondii* in the brains of mice 25 dpi with WT or *Δbfd1* parasites. Brain sections were stained with DBA and either anti-SAG1 antibody (top row) or anti-SRS9 antibody (bottom row). SAG1 or SRS9 (red); tdTomato (green); DBA (purple). Scale bar = 10 μm. Data are representative of 2 independent experiments. Data analyzed by two-sided unpaired Student's *t*-test; ns $p > 0.05$. Bar graphs depict the mean ± SD.

https://doi.org/10.1038/s41564-025-01967-z

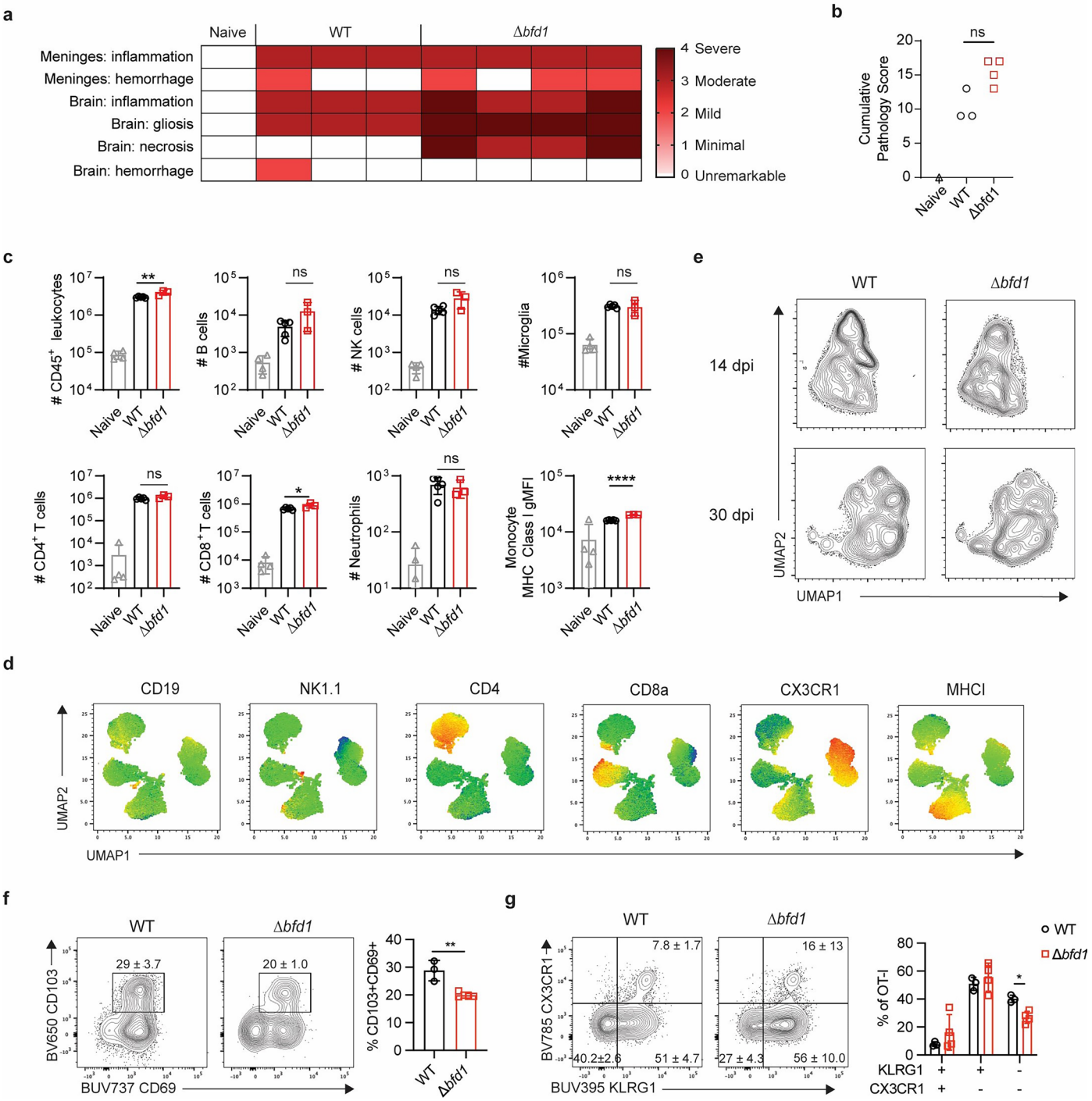

Extended Data Fig. 4 | Immune responses and pathology in the brain during chronic WT and *Δbfd1* infection. Brains were harvested from C57BL/6 J naïve mice and mice 30 dpi with WT or *Δbfd1* parasites and analyzed as described. **a**, Detailed semiquantitative pathological scoring of brain histology sections. **b**, Cumulative pathology score based on the parameters shown in **a** (WT, n = 3 mice; *Δbfd1*, n = 4 mice.) **c**,**d**, Flow cytometry analysis of brains from naïve mice (n = 4 mice) and mice at 30 dpi with WT (n = 5 mice) or *Δbfd1* (n = 3 mice) parasites (**p = 0.0093, *p = 0.0349, ****p = <0.0001; Data representative of 3 independent experiments). **c**, Quantification of CNS immune populations. **d**, Heatmaps displaying MFI of phenotypic markers used to identify UMAP clusters in Fig. 5e,f. **e**-**g**, Naive CD45.1+CD45.2+ OT-I T cells were transferred i.v. into mice 1 day prior to infection with WT (n = 3 mice) or *Δbfd1* (n = 4 mice) parasites. Brains were harvested and analyzed by flow cytometry (Data representative of 2 independent experiments.) **e**, UMAP analysis of OT-I T cells at 14 and 30 dpi. **f**, Frequency of CD69+CD103+ OT-I T cells at 30 dpi (**p = 0.0053.) **g**, KLRG1 and CX3CR1 expression on OT-I T cells at 30 dpi (*p = 0.016035.). Data analyzed by two-sided Mann-Whitney test (**b**) or two-sided unpaired Student's *t*-test (**c**,**f**,**g**); Bonferroni-Dunn correction for multiple comparisons was included in **g**; ns $p > 0.05$. Bar graphs depict the mean ± SD.

https://doi.org/10.1038/s41564-025-01967-z

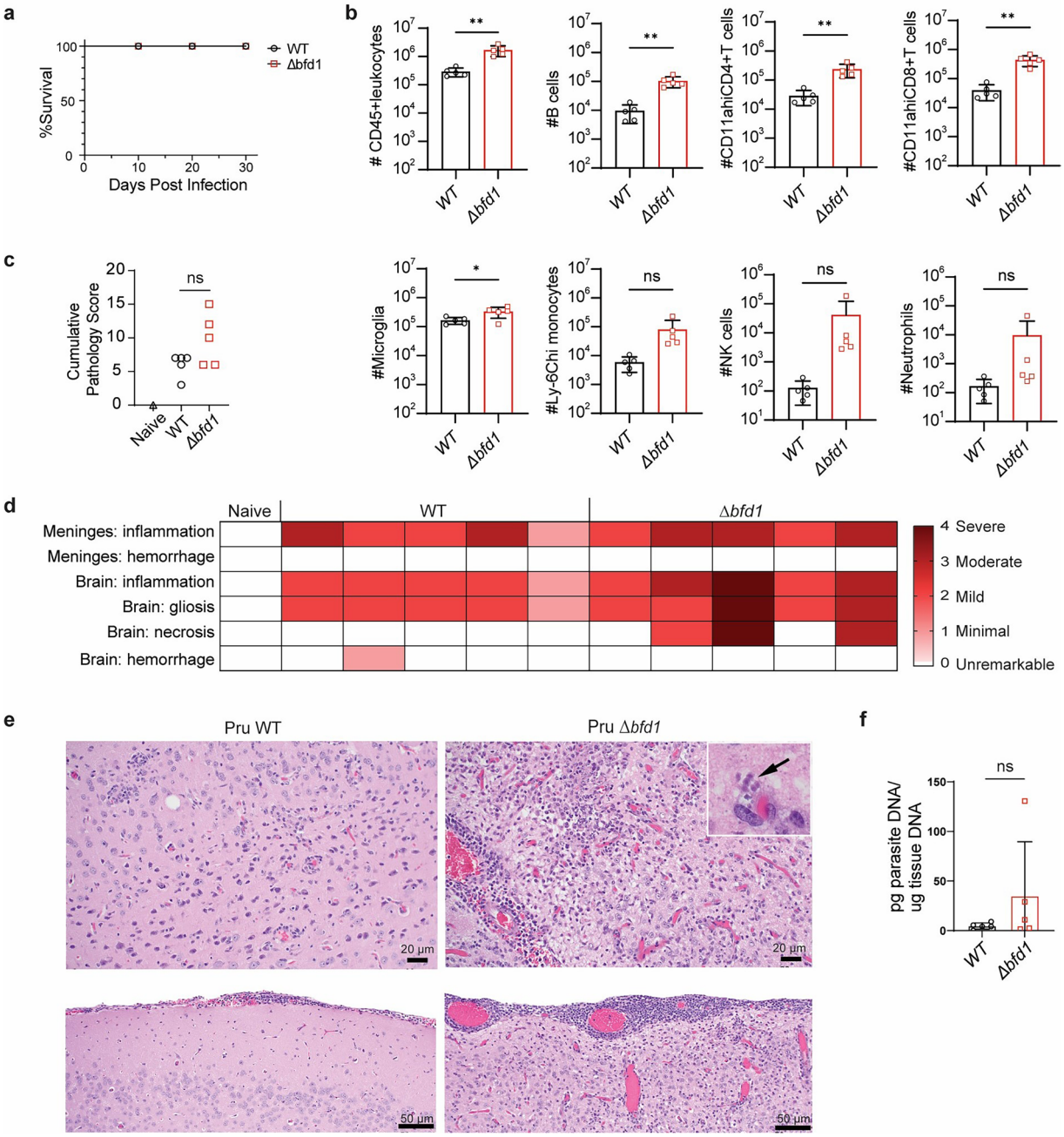

Extended Data Fig. 5 | CNS inflammation and pathology associated with *Δbfd1* infection across mouse and parasite strains. a-f, BALB/c mice were infected with WT or *Δbfd1* parasites. Brains were harvested and analyzed at 30 dpi. **a**, Survival of mice until time of harvest. **b**, Quantification of CNS immune cell populations measured by flow cytometry (in order of appearance: **p = 0.0020, **p = 0.0013, **p = 0.0039, **p = 0.0010, *p = 0.0299.) Gating scheme to identify CNS immune populations is depicted in Supplementary Fig. 6. **c**,**d**, Cumulative pathology score (**c**) and detailed pathological assessment (**d**) of brain histology sections. Assessment was performed by a board-certified veterinary pathologist. **e**, Representative photomicrographs of the brain showing the parenchyma (top) and meninges (bottom) in the cerebrum at 30 dpi. Inset and black arrow show tachyzoites in the brain during *Δbfd1* infection. **f**, Quantification of CNS parasite burden by qPCR. Data are representative of 1 experiment with n = 5 mice/group. Data analyzed by two-sided unpaired Student's *t*-test (**b**,**f**) or two-sided Mann-Whitney test (**c**); ns $p > 0.05$. Bar graphs depict the mean ± SD.

nature portfolio

Corresponding author(s): Christopher Hunter

Last updated by author(s): Jan 30, 2025

Reporting Summary

Nature Portfolio wishes to improve the reproducibility of the work that we publish. This form provides structure for consistency and transparency in reporting. For further information on Nature Portfolio policies, see our Editorial Policies and the Editorial Policy Checklist.

Statistics

For all statistical analyses, confirm that the following items are present in the figure legend, table legend, main text, or Methods section.

n/a	Confirmed	
☐	☒	The exact sample size (*n*) for each experimental group/condition, given as a discrete number and unit of measurement
☐	☒	A statement on whether measurements were taken from distinct samples or whether the same sample was measured repeatedly
☐	☒	The statistical test(s) used AND whether they are one- or two-sided *Only common tests should be described solely by name; describe more complex techniques in the Methods section.*
☒	☐	A description of all covariates tested
☐	☒	A description of any assumptions or corrections, such as tests of normality and adjustment for multiple comparisons
☐	☒	A full description of the statistical parameters including central tendency (e.g. means) or other basic estimates (e.g. regression coefficient) AND variation (e.g. standard deviation) or associated estimates of uncertainty (e.g. confidence intervals)
☐	☒	For null hypothesis testing, the test statistic (e.g. *F*, *t*, *r*) with confidence intervals, effect sizes, degrees of freedom and *P* value noted *Give P values as exact values whenever suitable.*
☒	☐	For Bayesian analysis, information on the choice of priors and Markov chain Monte Carlo settings
☒	☐	For hierarchical and complex designs, identification of the appropriate level for tests and full reporting of outcomes
☒	☐	Estimates of effect sizes (e.g. Cohen's *d*, Pearson's *r*), indicating how they were calculated

Our web collection on statistics for biologists contains articles on many of the points above.

Software and code

Policy information about availability of computer code

Data collection	Flow cytometry samples were collected using BD FACS DIVA v9.0 software, Microscopy images were collected and exported using Leica LAS X software (version 3.7.4.23463)
Data analysis	Graphs were made and Statistical tests were run in Prism 10.2.3 software (Graphpad), Flow cytometry analysis was performed using FlowJo versions 10.7.2 and 10.8.0 software. Fluorescent image analysis was performed using Zen 2.6 blue edition software and ImageJ version 1.53v. All code relating to the generation of ODEs are available on GitHub using the link provided: https://github.com/acwinn/TGondii

For manuscripts utilizing custom algorithms or software that are central to the research but not yet described in published literature, software must be made available to editors and reviewers. We strongly encourage code deposition in a community repository (e.g. GitHub). See the Nature Portfolio guidelines for submitting code & software for further information.

Data

Policy information about availability of data

All manuscripts must include a data availability statement. This statement should provide the following information, where applicable:

- Accession codes, unique identifiers, or web links for publicly available datasets
- A description of any restrictions on data availability
- For clinical datasets or third party data, please ensure that the statement adheres to our policy

Source Data files for Figures and Extended Data in this study are provided and listed in the Inventory of Supporting Information.

Research involving human participants, their data, or biological material

Policy information about studies with human participants or human data. See also policy information about sex, gender (identity/presentation), and sexual orientation and race, ethnicity and racism.

Reporting on sex and gender	No human participants or patient-derived materials were used in this study.
Reporting on race, ethnicity, or other socially relevant groupings	N/A
Population characteristics	N/A
Recruitment	N/A
Ethics oversight	N/A

Note that full information on the approval of the study protocol must also be provided in the manuscript.

Field-specific reporting

Please select the one below that is the best fit for your research. If you are not sure, read the appropriate sections before making your selection.

☒ Life sciences ☐ Behavioural & social sciences ☐ Ecological, evolutionary & environmental sciences

For a reference copy of the document with all sections, see nature.com/documents/nr-reporting-summary-flat.pdf

Life sciences study design

All studies must disclose on these points even when the disclosure is negative.

Sample size	Sample sizes were determined with an "n" of at least 3 individual mice per treatment group in order to estimate population variance for statistical testing, and sample size was scaled up based on strain, age, and sex matched cohort availability. Trends in the data were consistent and significant based on statistical testing.
Data exclusions	Mice that had succumbed to Toxoplasma infection were excluded from data collection and analysis (except for survival curves.) Only mice that had survived to the determined time of collection were euthanized and used for analysis.
Replication	All experiments in this study were repeated at least 2 times and the results replicated, with 2 exceptions: 1. Late chronic infection (6 month) with WT and bfd1KO parasites was performed once due to high rates of mortality in bfd1KO infection, limiting the availability of additional cohort of survivors for analysis. Repeats were attempted, but for humane and ethical reasons the mice were euthanized prior to the intended collection timepoint. Because of this, our main analyses were simply the presence or absence of parasites and our conclusion based on this experiment is that bfd1KO parasite persistence can occur; we do not perform more granular analyses comparing the infection groups. 2. Infection with BALB/c mice was performed once, and these data are only in an extended data figure.
Randomization	Randomization was not performed because age- and sex- matched cohorts were used and the animals are from inbred strains and therefore assumed to be genetically identical.
Blinding	Blinding was not possible for these experiments because data collection and analysis were performed by the same individuals.

Reporting for specific materials, systems and methods

We require information from authors about some types of materials, experimental systems and methods used in many studies. Here, indicate whether each material, system or method listed is relevant to your study. If you are not sure if a list item applies to your research, read the appropriate section before selecting a response.

Materials & experimental systems

n/a	Involved in the study
☐	☒ Antibodies
☐	☒ Eukaryotic cell lines
☒	☐ Palaeontology and archaeology
☐	☒ Animals and other organisms
☒	☐ Clinical data
☒	☐ Dual use research of concern
☒	☐ Plants

Methods

n/a	Involved in the study
☒	☐ ChIP-seq
☐	☒ Flow cytometry
☒	☐ MRI-based neuroimaging

Antibodies

Antibodies used

The following antibodies and reagents were used for staining: B220: BUV496, BD Biosciences: 612950, clone: RA3-6B2, RRID:AB_2870227, dilution 1:300; CD3: APC-ef780, Invitrogen: 47-0032-82, clone: 17A2, RRID:AB_1272181, dilution 1:300; CD3: BUV737, BD Biosciences: 612803, clone: 17A2, RRID:AB_2738781, dilution 1:300; CD3e: PE-cf594, BD Biosciences: 562286, clone: 145-2C11, RRID:AB_11153307, dilution 1:300; CD4: BUV496, BD Biosciences: 612952, clone: GK1.5, RRID:AB_2813886, dilution 1:200; CD4: BV650, Biolegend: 100555, clone: RM4-5, RRID:AB_2562529, dilution 1:400; CD4: FITC, eBioscience: 11-0041-85, clone: GK1.5, RRID:AB_464892, dilution 1:200; CD4: APC-ef780, Invitrogen: 47-0041-82, clone: GK1.5, RRID:AB_11218896, dilution 1:300; CD8a: BUV563, BD Biosciences: 748535, clone: 53-6.7, RRID:AB_2872946, dilution 1:200; CD8a: BUV615, BD Biosciences: 613004, clone: 53-6.7, RRID:AB_2870272, dilution 1:200; CD8a: BV650, Biolegend: 100742, clone: 53-6.7, RRID:AB_2563056, dilution 1:200; CD8b: APC-ef780, Invitrogen: 47-0083-82, clone: eBioH35-17.2, RRID:AB_2573943, dilution 1:200; CD11a: BUV805, BD Biosciences: 741919, clone: 2D7, RRID:AB_2871232, dilution 1:300; CD11b: BV650, Biolegend: 101259, clone: M1/70, RRID:AB_2566568, dilution 1:500; CD19: BUV395, BD Biosciences: 563557, clone: 1D3, RRID:AB_2722495, dilution 1:300; CD45: AF647, Biolegend: 103124, clone: 30-F11, RRID:AB_493533, dilution 1:200; CD45.1: ef450, Invitrogen: 48-0453-82, clone: A20, RRID:AB_1272189, dilution 1:200; CD45.1: BV711, Biolegend: 110739, clone: A20, RRID:AB_2562605, dilution 1:200; CD45.1: PE-Cy7, Biolegend: 110730, clone: A20, RRID:AB_1134168, dilution 1:200; CD45.2: APC, Biolegend: 109814, clone: 104, RRID:AB_389211, dilution 1:200; CD45.2: BV711, Biolegend: 109847, clone: 104, RRID:AB_2616859, dilution 1:200; CD69: BUV737, BD Biosciences: 612793, clone: H1.2F3, dilution 1:200; CD69: PerCP-Cy5.5, eBioscience: 45-0691-82, clone: H1.2F3, RRID:AB_1210703, dilution 1:400; CD103: PE, eBioscience: 12-1031-81, clone: 2E7, RRID:AB_11150242, dilution 1:200; CD103: BV605, Biolegend: 121433, clone: 2E7, RRID:AB_2629724, dilution 1:200; CD107a: PE-Cy7, Biolegend: 121620, clone: 1D4B, RRID:AB_2562146, dilution 1:300; CD127: BV421, Biolegend: 135027, clone: A7R34, RRID:AB_2563103, dilution 1:200; CTLA-4: APC-R700, BD Biosciences: 565778, clone: UC10-4F10-11, RRID:AB_2739350, dilution 1:200; CX3CR1: BV785, Biolegend: 149029, clone: SA011F11, RRID:AB_2565938, dilution 1:400; CX3CR1: PerCP-Cy5.5, Biolegend: 149009, clone: SA011F11, RRID:AB_2564493, dilution 1:400; F4/80: APC-ef780, eBiosciences: 47-4801-82, clone: BM8, RRID:AB_2735036, dilution 1:200; GFP: AF488, Biolegend: 338008, clone: FM264G, RRID:AB_2563288, dilution 1:300; H-2Kb: AF647, Biolegend: 116512, clone: AF6-88.5, RRID:AB_492917; I-A/I-E: AF700, Biolegend: 107622, clone: M5/144.15.2, RRID:AB_493727, dilution 1:300; I-A/I-E: BV711, Biolegend: 107643, clone: M5/144.15.2, RRID:AB_2565976, dilution 1:1200; IFN-γ: BUV737, BD Biosciences: 612769, clone: XMG1.2, dilution 1:200; Ki-67: BV470, BD Biosciences: 566109, clone: B56, RRID:AB_2739511, dilution 1:200; KLRG1: BUV395, BD Biosciences: 740279, clone: 2F1, RRID:AB_2740018, dilution 1:200; Ly-6C: BV785, Biolegend: 128041, clone: HK1.4, RRID:AB_2565852, dilution 1:600; Ly-6G: BUV563, BD Biosciences: 612921, clone: 1A8, RRID:AB_2870206, dilution 1:400; NK1.1: BUV395, BD Biosciences: 564144, clone: PK136, RRID:AB_2738618, dilution 1:300; PD-1: BV421, Biolegend: 135221, clone: 29F.1A12, RRID:AB_2562568, dilution 1:200; PD-1: BV605, Biolegend: 135220, clone: 29F.1A12, RRID:AB_2562616, dilution 1:200; PD-1: BV785, Biolegend: 135225, clone: 29F.1A12, RRID:AB_2563680, dilution 1:200; T-bet: AF647, Biolegend: 644804, clone: 4B10, RRID:AB_1595466, dilution 1:200; TCRβ: PerCP-Cy5.5, Biolegend: 109228, clone: H57-597, RRID:AB_1575173, dilution 1:500; TCRβ: ef450, Invitrogen: 48-5961-82, clone: H57-597, RRID:AB_11039532, dilution 1:200; Tetramer MHCI (OVA): PE, NIH Tetramer Core, peptide: SIINFEKL, dilution 1:300; Tetramer MHCI (Tgd057): APC, NIH Tetramer Core, peptide: SVLAFRRL, dilution 1:300; Tetramer MHCII (AS15): APC, NIH Tetramer Core, peptide: AVEIHRPVPGTAPPS, dilution 1:400; Tim3: BV605, Biolegend: 119721, clone: RMT3-23, RRID:AB_2616907, dilution 1:200; TNF-α: APC, Invitrogen: 17-7321-82, clone: MP6-XT22, RRID:AB_469508, dilution 1:200; Vα2 TCR: BUV615, BD Biosciences: 751416, clone: B20.1, RRID:AB_2875415, dilution 1:400; Vα2 TCR: PE, Biolegend: 127808, clone: B20.1, RRID:AB_1134183, dilution 1:300; Viability: GhostDye Violet 510, TONBO Biosciences: 13-0870-T100, dilution 1:300; Viability: GhostDye Red 780, TONBO Biosciences: 13-0865-T100, dilution 1:300. anti-OVA, Abcam: ab181688, dilution 1:200; DBA, Vector laboratories: B1035, dilution 1:500; anti-GFAP, DAKO: Z0334, dilution 1:200; anti-MAP2, Abcam: ab5392, dilution 1:2000; anti-NeuN, Millipore: MAB3778, dilution 1:200; anti-Neurofilament, Abcam: ab4680, dilution 1:20,000.

Validation

All flow cytometry antibodies used in this study are established and well cited by the manufacturer (BD Biosciences, Invitrogen, eBiosciences, Biolegend) and were validated by the manufacturer using flow cytometry on primary mouse cells: "verified by Relative expression and Cell treatment to confirm specificity to [the target]." Imaging antibodies used in this study for imaging are established, validated, and cited by the manufacturer. Antibodies against GFAP, MAP2, NeuN, and Neurofilament were validated by immunohistochemistry on primary mouse or rat glial cells or cortical neurons. The antibody against OVA was validated by western blot staining by the manufacturer. Further information and validation for specific antibodies can be found on the manufacturers' website.
Polyclonal rabbit anti-Toxoplasma antibody used for parasite detection in histology - Conley FK, Jenkins KA, Remington JS. Toxoplasma gondii infection of the central nervous system. Use of the peroxidase-antiperoxidase method to demonstrate toxoplasma in formalin fixed, paraffin embedded tissue sections. Hum Pathol. 1981 Aug;12(8):690-8. doi: 10.1016/s0046-8177(81)80170-0. PMID: 7026410.

Eukaryotic cell lines

Policy information about cell lines and Sex and Gender in Research

Cell line source(s)	Commercially available human foreskin fibroblast cells (HFF-1) derived from a male donor were used. T. gondii strains used in this study have been previously published.
Authentication	HFF-1 cells were authenticated by the source. T. gondii strains were validated in original publications by PCR and sequencing, and OVA and fluorescent reporter expression was confirmed by flow cytometry in this study.
Mycoplasma contamination	Cell lines tested negative for Mycoplasma contamination using the MycoScope PCR Mycoplasma Detection Kit (Genlantis cat no: MY01050)
Commonly misidentified lines (See ICLAC register)	No misidentified cell lines were used in this study.

Animals and other research organisms

Policy information about studies involving animals; ARRIVE guidelines recommended for reporting animal research, and Sex and Gender in Research

Laboratory animals	Mice were housed in the University of Pennsylvania Department of Pathobiology vivarium according to institutional guidelines with 12-hour light/dark cycles, ambient temperature ranging from 68^{0}F – 77^{0}F, and ambient humidity ranging from 35% - 55%. C57BL/6J (stock no: 000664, RRID:IMSR_JAX:000664), CD45.1 (B6.SJL-Ptprca Pepcb/BoyJ, stock no: 002014, RRID:IMSR_JAX:000664), Nur77GFP (Stock no: 016617, RRID:IMSR_JAX:016617), OT-I (Stock no: 003831, RRID:IMSR_JAX:003831), and BALB/c (Stock no: 000651, RRID:IMSR_JAX:000651) mice were purchased from Jackson Laboratories and bred at the University of Pennsylvania. Snap25Cre mice were generously provided by Hongkui Zeng at the Allen Institute for Brain Science and Stat1Flox mice were generously provided by Lothar Hennighausen at the National Institutes of Health and published previously (Klover PJ, Muller WJ, Robinson GW, Pfeiffer RM, Yamaji D, Hennighausen L. Loss of STAT1 from mouse mammary epithelium results in an increased Neu-induced tumor burden. Neoplasia. 2010 Nov;12(11):899-905. doi: 10.1593/neo.10716.) Mice were infected at 8 weeks of age.
Wild animals	No wild animals were used in this study.
Reporting on sex	Male mice were used in these studies.
Field-collected samples	No field-collected samples were obtained for this study.
Ethics oversight	Ethical oversight of all animal studies was approved by the University of Pennsylvania Institutional Care and Use Committee (protocol #805045).

Note that full information on the approval of the study protocol must also be provided in the manuscript.

Plants

Seed stocks	N/A
Novel plant genotypes	N/A
Authentication	N/A

Flow Cytometry

Plots

Confirm that:

☒ The axis labels state the marker and fluorochrome used (e.g. CD4-FITC).

☒ The axis scales are clearly visible. Include numbers along axes only for bottom left plot of group (a 'group' is an analysis of identical markers).

☒ All plots are contour plots with outliers or pseudocolor plots.

☒ A numerical value for number of cells or percentage (with statistics) is provided.

Methodology

Sample preparation	To generate single cell suspensions from murine tissues for flow cytometry, spleens were passed through a 40□m filter and red blood cells were lysed for 3 minutes at room temperature in ACK lysis buffer. Brains were diced into 1mm pieces and digested at 37C 5% CO2 for 1.5 hours with 250ug/mL collagenase/dispase and 10□g/mL DNase, and then passed through a 70 □m filter. Leukocytes were then isolated through a 30% and 60% percoll gradient and density centrifugation at 2000rpm for 25 minutes. Whole blood was collected through submandibular bleed into 0.05mM EDTA in PBS. Cells were pelleted and red blood cells were lysed for 3 minutes at room temperature in ACK lysis buffer.
Instrument	Stained cells were acquired on a BD LSR Fortessa, BD FACSymphony A5, or BD FACSymphony A3
Software	Flow cytometry sample collection was performed using BD FACS DIVA v9.0. Analysis was performed using FlowJo versions 10.7.2 and 10.8.0 software
Cell population abundance	OT-I T cells were between 0.1 and 30% of activated CD8 T cells in the brain during infection with bag1-OVA or tub1-OVA parasites, respectively.
Gating strategy	All samples were gated on Lymphocytes (FSC-A X SSC-A) --> Single cells (FSC-H x FSC-W then SSC-H x SSC-W) --> Live (Viability dye negative. All gates for stained samples were determined based on control samples stained with all fluorescent antibodies used in the flow panel except the marker of interest (FMO) for each antibody. Gating strategies for identifying OT-I T cells and general immune phenotyping can be found in Extended Data Figures 1d and 4, respectively.

☒ Tick this box to confirm that a figure exemplifying the gating strategy is provided in the Supplementary Information.